Electromagnetic Field Induced Crack Driving Force and Two Failure Mechanisms of Conductors with Defect: Melting-Induced Softening and Electric-Breakdown

S. Hao[1,2] , Q. Wang, L. M. Keer
[1] Dept. Mech. Engr., Northwestern University, Evanston, IL 60208, U. S. A.
[2]ACII Consulting, Wilmette, IL 60091, U. S. A.
hao0@suhao-acii.com, suhao@northwestern.edu

Abstract

In material's selection and design of magnetic transmission system or MEM/NEM device, a crucial issue is to identify the failure mechanism of a conductor component with defects or a contact between conductors under a combination of electrical, magnetic, and mechanical loads. When externally applied mechanical load is very small or vanishes, electric-breakdown and localized melting, e.g. at a crack tip, caused by resistance induced energy dissipation, are the two major processes that may lead to failure. In order to quantitatively identify the critical conditions for these two competing mechanisms, close-formed mean field solutions of conductor plate with defect in the form of crack have been obtained through solving Maxwell's equations, momentum conservation, and heat conduction equation. For two dimensional problems, a general solution of the magnetic field associated with in-plane electrical current has been derived using conjugate function. Therefore the corresponding Lorentz' force and stress intensity factor can be computed analytically; which have remarkable effects on processes of material's failure. Under the framework of the semi-classical theory of metals, mean free path of electron flow and the interactions between electron and impurities have also been discussed, where the former defines a length parameter to link macroscale analysis with underlying atomistic physics through electrical conductivity. The obtained mean field solutions, in conjunction with Paschen law, lead to the solution of the threshold of applied electrical load at breakdown and associated energy dissipation; the latter represents the "fracture toughness" under this critical condition. These solutions also indicate that there three patterns of electrical breakdown regarding the location where it happens, depending upon crack tip geometry, material's properties, and the level of applied mechanical load. The condition for crack tip breakdown, the distance to crack when breakdown occurs away from a crack tip, and the threshold of applied electrical load have been obtained analytically. By comparing the energy dissipations of breakdown and crack tip melting, a "material's constant" has been derived based on a proposed circuit model to distinguish these two competing mechanisms, which defines a criterion to predict the dominating process for a given conductor.

Key words: Lorentz force, magnetic, electric-breakdown, defect, crack, crack growth, failure mechanism, stress intensity factor, fracture toughness, dislocation, impurity, multi-physics, length scale, Maxwell equation.

1. Introduction

The theory of electrodynamics indicates that on a concave solid surface, electric-breakdown may occur if the distance between two adjacent surfaces, such as the two edges of a crack tip, is smaller than a certain critical value when an electric field is applied [1-3]. For a dielectric medium containing an elliptical inclusion with different dielectric coefficient, a quantitative analysis was performed in [4] to obtain critical amplitude of electric field remotely applied.

A defect in a solid conductor is a geometric discontinuity, which can be an ellipsoid cavity or a crack containing either a dielectric phase or another conduct with different conductivity. Although a crack is the extreme case of an ellipsoid, a sharp crack with very small radius at tip causes extremely high energy concentration [1-2] that highlights the underlying mechanisms from different scales at localized area, by which the enhanced phenomena may not be fully covered by ellipsoid's solution. Experimental evidences indicate that a cracking-induced material's failure in a conductor under electromagnetic loading is a process with complicated underlying mechanisms. Fig. 1 shows an observation of crack growth and melting at the crack tip under a pulsing electric load [5]. For such a configuration, when a magnetic field simultaneously presents along the direction not parallel to electric current, the corresponding Lorentz force can be remarkably high which separates the opposite crack surfaces. A pulse electrical potential induced skin effect may ionize the surfaces, leading to high electric dipole density near the crack tip with repulsive London's force. The combination of London and Lorentz forces, in conjunction with the possible surface charge-induced Columon's force, may produce a very high stress-intensity factor that drives crack to grow. On other hand, an electric-breakdown or high amplitude of electric current is accompanied with significant energy dissipation, which causes high temperature gradient within localized area where the material will lose its resistance against fracture due to thermal softening and melting [5, 6]. Eventually this multi-physics process will finally end by crack propagation and subsequent structural failure. Hence, it is crucial to obtain the critical conditions of melting, electric-breakdown, and crack growth in such a defected conductor, so as to ensure enough safety margin of applied load in machines, devices, and materials' designs.

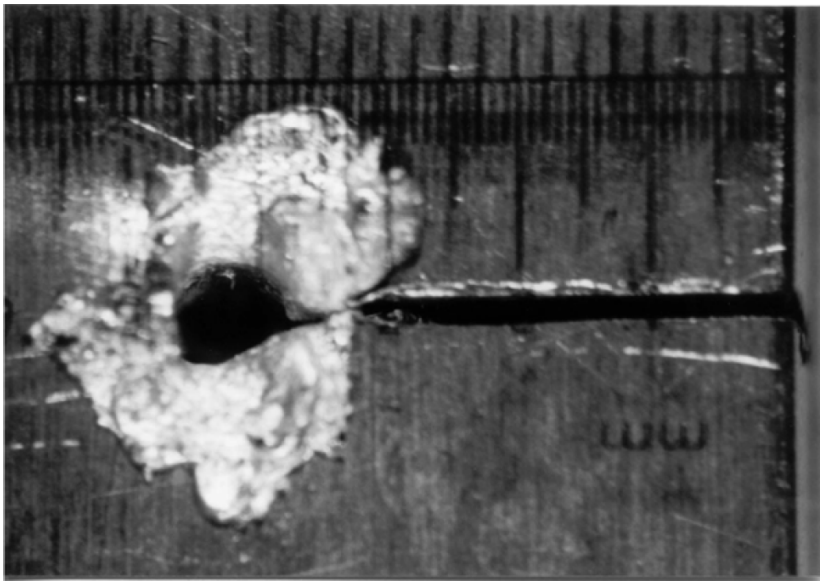

Fig. 1 An observation of the melted crack tip after electric-breakdown [5]

By tracking literatures, e.g. [7-10, 19, 48, 49, 52, 53, 58-65], one can find increasing interests and accumulated research reports with many successful applications for the problems coupling mechanical and electromagnetic loads, when electric or magnetic field-induced displacement causes significant mechanical deformation. A model theory of stress-induced magnetization for ferromagnetic materials has been developed in [10]. The interaction between magnetic hysteresis and stress field has been studied in [58,59]. In continuum theory of piezoelectric and piezomagnetic matters, the mechanical response is usually mathematically represented through constitutive law, e.g. strain tensor becomes a function of both mechanical stress and generalized electric and magnetic "stresses"; see e.g. [61,63]. When this kind of constitutive law is linear, closed-formed theoretical solutions and detailed analysis have been conducted for various materials with cracked-geometries [11-15, 19, 54, 61-66].

The paper studies the conditions of electric-breakdown and melting of linear elastic conductor with crack under electrical and magnetic load; whereby the challenges lie in its multi-physics nature and the nonlinearity associated with Lorentz force, although linear approximations are made for each individual mechanism. This is because Lorentz force is the cross product of electric and magnetic fields so the corresponding mechanical equilibrium condition (moment conservation) is nonlinear for linear elastic solid. When dissipation-induced melting occurs, the effect of solid-liquid phase transformation has to be taken into account. In many cases these nonlinearities can be ignorable. However, when geometric discontinuities, such as cracks, present, the effect of this coupling-induced nonlinear force may become crucial.

The analysis in this paper is presumed under static electrical load. The obtained results may also be suitable for dynamic problems if the corresponding deformation scale, e.g. crack opening displacement, is much smaller than the involved time-dependent length scales such as the wave length of the involved electromagnetic wave [2]. Also, as indicated in [1], when the electric conductivity and dielectric coefficient are constants, the solution structure of static electric field for conductors is identical to that for dielectric materials. This is because the both cases obey the same Laplace equation except at the interface between different materials. Further more, according to the semi-classical theory of metals [16], the macro-scale conductivity is a function of mean free path of electron, which defines a length parameter to link mean field analysis, e.g. Maxwell's equation's solutions, to the atomistic physics such as dislocation mechanisms. By presuming diluted-distributed point defects in the form of screw dislocation and misfit solution atoms, the asymptotic expression of this length parameter has been studied. It also defines the lower bound for the applicability of obtained mean-field solutions.

This paper is organized as following: next section introduces the governing equations and boundary conditions for the problems to be studied in the framework of macroscopic mean-field theories. Section III introduce a series of two-dimensional solutions which includes three parts: a general solution of magnetic field associated with any electrical field; electrical field solutions for crack and hole problems with and without breakdown; and asymptotic solution of Lorentz force induced stress intensity factor. In Sections IV an asymptotic temperature field solution including a melting zone around a crack tip has also been derived By comparing energy dissipations caused by melting and breakdown, a capacitance-resistance circuit model is proposed to distinguish dominant mechanism. In section V this circuit model, in conjunction

with Paschen's law, leads to the predictions of a critical condition of breakdown and associated energy dissipation; the former defines a "threshold" of applied electric field; the latter provides an estimate of the material's "fracture toughness" against breakdown-induced failure. Also, based on the framework of the semiclassical theory of conducting metals, the interactions between electron transport and three kinds of diluted impurities have been studied, by which an asymptotic solution of electron free path, the length parameter to link macroscopic solutions and underlying mechanisms, has been obtained. Finally a dimensionless material constant, defined as the ratio between the energy dissipations of breakdown and melting, is suggested based on the obtained analytical solutions; which can be used to predict the dominant failure mechanism of conduct under electrical magnetic load for a given conductor.

Standard notation is used throughout. The boldface symbols denote tensors; the order of a tensor is indicated by the context. Plain symbols denote scalars or components of a tensor when a subscript is attached. Symbol z_3 represents the coordinate perpendicular to the $\{x, y\}$ plane in a three-dimensional Cartesian system $\{x, y, z_3\}$, whereas "z" is a complex variable $z = x + iy$ with $i = \sqrt{-1}$. For a complex function $F(z) = u(x, y) + iv(x, y)$, its conjugate function $\overline{F}(z) = u(x, y) - iv(x, y)$. The SI unit is used throughout the text except otherwise specified.

2. Governing Equations, Boundary Conditions and Approximations

Figure 2 is a schematic showing the problem to be analyzed, where a conductor with electric conductivity σ^C contains an ellipsoid inclusion with dielectric coefficient ε_1. In this diagram, μ and v are Young's module and Possion's ratio, respectively; symbols ***E, J, D, H, B*** denote the macroscopic electric field, current density, electric displacement, macroscopic magnetic field, and magnetic induction field. All symbols and variables associated with the ellipsoid inclusion are denoted by subscription "1".

2.1 Lorentz Force, Maxwell's Equations, Moment Conservation and Heat Conduction

The primary governing equation for the problems studied is the momentum conservation (force equilibrium condition) at each material point whereby the Lorentz force presents as body force terms on the right hand side:

$$\nabla \cdot \boldsymbol{\sigma} = \rho_m \frac{\partial^2 \boldsymbol{u}}{\partial t^2} - \rho_e \left(\boldsymbol{E} + \boldsymbol{v}_q \times \boldsymbol{B} \right) \tag{1}$$

where ∇ is differential gradient operator, **σ** is stress tensor, **u** is deformation displacement tensor; ρ_e and ρ_m are the free charge density and mess density per unit volume, respectively; $\boldsymbol{v}_q$ is the velocity of the electric charge so $\rho_e \boldsymbol{v}_q = \boldsymbol{J}$ is current density; $\boldsymbol{E}$ and $\boldsymbol{B}$ are the macroscopic electric field and magnetic induction field, respectively, determined by Maxwell Equations. Hence, on the right hand side of (1) the term "$-\rho_m \frac{\partial^2 \boldsymbol{u}}{\partial t^2}$," represents inertia, the term "$\rho_e \boldsymbol{E}$ "is electrical force whereas the term $\rho_e \boldsymbol{v}_q \times \boldsymbol{B} = \boldsymbol{J} \times \boldsymbol{B}$ is magnetic force.

Presently only the time-independent problems are studied whereas the frequency-dependent problem will be discussed in following research reports. Under this condition, the Maxwell Equations to be solved are these as below:

$$\begin{aligned} &\text{I.} && \nabla \cdot \boldsymbol{B} = 0 \\ &\text{II.} && \nabla \times \boldsymbol{E} = 0 \\ &\text{III.} && \nabla \cdot \boldsymbol{D} = \rho_E \\ &\text{IV.} && \nabla \times \boldsymbol{H} = \boldsymbol{J} \end{aligned} \qquad (2)$$

where ρ_E is the density of charge sources. In this study, $\rho_E = 0$, and the following linearized constitutive relations apply [1, 2]:

$$\mathbf{D} = \varepsilon \mathbf{E} \qquad (3a)$$

$$\boldsymbol{B} = \mu_M \boldsymbol{H} \qquad (3b)$$

, and in a conductive material:

$$\boldsymbol{J} = \rho_e \boldsymbol{v}_q \qquad (4)$$

with the Ohm's Law at each material point:

$$\boldsymbol{J} = \sigma^C \boldsymbol{E} \qquad (5)$$

In (3a,b) and (5), the dielectric coefficient ε, magnetic permeability μ_M, and electric conductivity σ^C are assumed to be constants. In this analysis, only the magnetic field induced by electric field is taken into account. Under this condition, the coupling of magnetic field on electric field, e.g. the Hall effect, is about 3 to 4 orders smaller than the non-coupling parts [11] and is omitted.

Remark: The constitutive relations between the pair $(\boldsymbol{D}, \boldsymbol{E})$ and $(\boldsymbol{B}, \boldsymbol{H})$ are nonlinear for most materials [1, 2, 16]; the dielectric coefficient and magnetic permeability are tensors in general. The relations (3a,b) imply the approximations of isotropic magnetic electrical materials leaving out the effects of (i) magnetic hysteresis; (ii) the coupling between magnetic and electrical fields (Hall effect); (iii) magnetic and the electrical polarizations on conductor's surfaces. The studies about interaction between magnetic hysteresis and mechanical stress field can be found, e.g. in [58, 59,67]. Introductions about Hall effect can be found, e.g. in [16].

For the linear elastic solid studied in this paper, the stress tensor, $\boldsymbol{\sigma}$, and the displacement field, **u,** are correlated each other through the linear Hook's law under the approximation of small strain:

$$\boldsymbol{\sigma} = \boldsymbol{C}^e : \boldsymbol{e} \qquad \boldsymbol{e} = \nabla \boldsymbol{u} + \nabla^T \boldsymbol{u} \qquad (6)$$

where $\mathbf{C}^e$ is the elastic stiffness tensor.

Heat conduction and the associated temperature field, *T,* is governed by Fock's law:

$$k_h \nabla^2 T + \rho_H = 0 \tag{7}$$

where ρ_H is a heat source and k_h the thermal conductivity. Heat convection through the surface is neglected. In this analysis, the Wiedemann-Franz relation applies [16]:

$$k_h = \frac{3}{2}\sigma^C T\left(\frac{k_B}{e}\right)^2 \tag{8}$$

where k_B is the Boltzman's constant, and $e = 1.60319E-19$ *Coulumb* which is the charge carried by an electron. (8) gives the relationship between thermal conductivity k_h and electric conductivity σ^C.

2.2 Boundary Conditions

Fig. 2 illustrates a two-body system where a large conductor contains a defect, e.g. an ellipsoid. As a convention, one may define surface change density ρ_S and surface current density vector $\boldsymbol{K}$ at the interface between the two materials. As a convention, the outer normal of interface surface always points to the inclusion, as illustrated in Fig. 2. The corresponding current and electromagnetic boundary conditions at the interface between the matrix and the defect read [1,2]:

$$\boldsymbol{n}\cdot(\boldsymbol{J}-\boldsymbol{J}_1)=\rho_S \tag{9a}$$

$$\boldsymbol{n}\cdot(\boldsymbol{H}-\boldsymbol{H}_1)=0, \qquad \boldsymbol{n}\times(\boldsymbol{H}-\boldsymbol{H}_1)=\boldsymbol{K} \tag{9b}$$

where the subscription "1" denotes the quantities in the defect side. Assuming a traction $\boldsymbol{T}$ on a boundary segment denoted as Γ_t, the corresponding force boundary condition reads:

$$\boldsymbol{T}=\boldsymbol{n}\cdot\boldsymbol{\sigma} \qquad \text{on} \quad \Gamma_t \tag{9c}$$

When a displacement field $\bar{\mathbf{u}}$ is given on a boundary segment denoted as Γ_u, the corresponding displacement boundary condition reads:

$$\bar{\boldsymbol{u}}=\boldsymbol{u} \qquad \text{on} \quad \Gamma_u \tag{9d}$$

On the interface between the matrix and the defect:

$$\boldsymbol{n}\cdot(\boldsymbol{\sigma}-\boldsymbol{\sigma}_1)=0, \qquad \boldsymbol{u}-\boldsymbol{u}_1=\boldsymbol{0} \tag{9c}$$

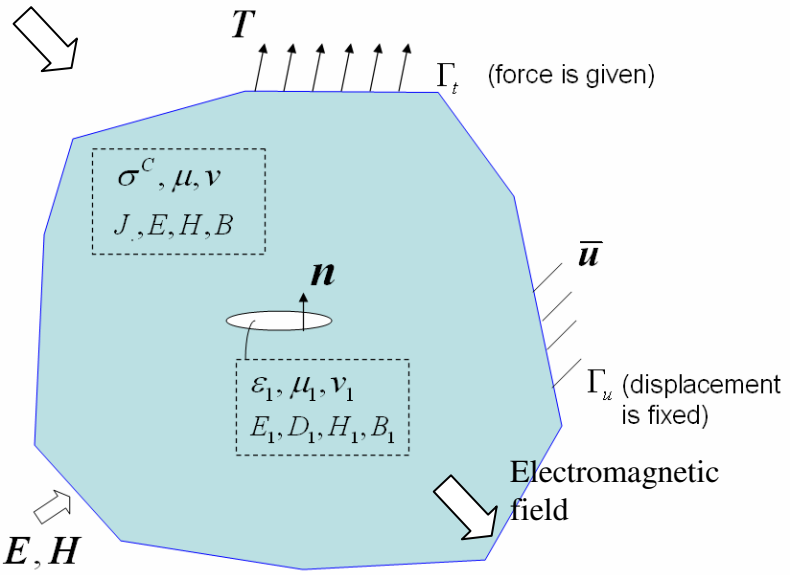

Fig. 2 A conducting solid body containing a dielectric cavity, where ε, μ, v are the dielectric coefficient, Young's module and Possion's ratio, respectively. The corresponding interfacial and boundary conditions are described by (9a-9d).

2.3 Two-dimensional approximations: Plane Strain and Plane Stress

Field solutions of a conductor, such as the matrix material in Fig. 2 under an applied electric field at remote, are to be studied under the two-dimensional "plane stress" and "plane strain" approximations, which can be considered as the two extreme cases of three-dimensional problem, explained as follows:

(1) Plane-strain condition: a plate contains one or more cylinder ellipsoid(s) with their axes perpendicular to the $\{x, y\}$ plane that defines the plate; External applied electrical, magnetic, mechanical force, and displacement fields may act on the plate's boundaries; all these external fields are independent of z_3, the coordinate perpendicular to plate; they have only the components within $\{x, y\}$ plane except magnetic field. When the thickness of the plate is much greater than the long axis length of these ellipsoids, the middle part along the plate thickness is under the "plane strain" condition. In addition to the governing equations (1)-(10), "plane strain" condition is mathematically described by:

$$J_3 = E_3 = 0; \qquad e_{33} = e_{x3} = e_{y3} = 0 \tag{10a}$$

where J_3 and E_3, respectively, are the components of current and electric field along z_3 direction; e_{i3} are the components of strain tensor defined by (6). In (10a) and the following analysis, both subscripts "z_3" and "3" stand for the variables associated with coordinate z_3 perpendicular to the $\{x, y\}$ plane.

(2) Plane-stress condition: all requirements for the plane strain are satisfied except the thickness of the plate which is so thin that, instead of (10a), the following conditions are met:

$$J_3 = E_3 = 0; \qquad \sigma_{33} = \sigma_{x3} = \sigma_{y3} = 0 \tag{10b}$$

where σ_{i3} are the components of stress tensor. Additionally, it is assumed that the first-order derivatives of electric and magnetic fields along z_3 direction are zero within the plate and no surface concentration and polarization for any field variables except strain; hence, in the plate the following relation is applicable:

$$\mu_M H_3 = \mu_M^0 H_3^0 \tag{10c}$$

where μ_M^0 and H_3^0 are the magnetic permeability in the space out of the plate and the corresponding magnetic field, respectively.

Under plane stress or plane strain approximation, substituting (10a) or (10b) into Maxwell's equation I and IV of (2):

$$\frac{\partial H_x}{\partial x} + \frac{\partial H_y}{\partial y} = 0, \qquad \frac{\partial H_x}{\partial y} - \frac{\partial H_y}{\partial x} = 0 \qquad \text{thus} \qquad \nabla^2 H_x = \nabla^2 H_y = 0 \tag{10d}$$

which defines an analytical function $H_{//} = H_x + iH_y$ where i is imaginary number: $i = \sqrt{-1}$. In this study a further approximation is no external applied fields of H_x and H_y for the problem addressed in Fig. 2. Thus, the following trivial solutions is taken in the following analysis:

$$H_x = H_y = 0 \tag{10e}$$

Hence, the problem to be dealt with can be stated as a plane stress or plane strain infinite large plate with the constant σ^C, μ and v, which contains a through dielectric cylinder in the shape of ellipsoid or crack with the coefficients ε_1, μ_1 and v_1, as those illustrated in Fig. 4. In this study the dielectric cylinder is gas while the plate is metal, so $\mu_1 \approx 0$ and $v_1 \approx 0$. The metal plate contains no free charge or charge source, subjected to a constant uniform electric current at infinite:

$$J_x = E_x = 0, \quad J_y = \sigma^C E_y = -\sigma^C E^\infty \qquad \text{when} \quad \sqrt{x^2 + y^2} \to \infty \tag{10f}$$

For a plate conductor with finite thickness, its mechanical field is somewhere in-between plane stress and plane strain solutions. When $|H_x| << |H_3|$, $|H_y| << |H_3|$ and $J_3 = 0$ on the plate's surfaces, there is no essential difference between plane stress and plane strain solutions of magnetic and electrical fields after the effect of magnetic susceptibility is taken into account for finite thickness.

2.4 Definition of "Crack" – Sharp and Blunted Crack Tips

The defect's geometry in a conductor can be distinguished into two classes, ellipsoids and cracks. The former can be dielectric inclusion or gas pore; the latter represents a geometric discontinuity, e.g. separation of grain boundary or other kinds of interfaces. Although mathematical a crack with sharp tip can be considered as the degenerated case of the ellipsoid, however, it is difficult to use ellipsoid to describe a long crack with blunted tip, the associated physical phenomena within the local area around the blunted tip can also be very different.

Experimental observations indicate that crack tips in engineering materials are always blunted. For a metal that obeys conventional elastic, perfectly-plastic stress-strain law under plane strain condition, blunting of a sharp crack tip can be quantified by the slip-line field solutions illustrated in Figs. 3a,b. When remote applied stress σ^{∞} is much smaller than the material's yield stress, the corresponding stress, strain and deformation in the close vicinity of a sharp crack tip are described by the Prandtl's field solution [22, 68] plotted in Fig. 3a. Blunting appears when σ^{∞} increases; the near crack tip field solution is given by the Rice-Johnson-Prandtl's field in Fig. 3b; where the sharp tip becomes a semi-circle configuration that connects to the two parallel crack wedges. The specified solutions obtained in [68] applies for the shaded area ahead the blunted semi-circle tip in Fig. 3b, which has the similar structure as the slip-line field around a hole of the radius r_b but is confined by the Prandtl's field solution presented in Fig. 3a. Although strain-hardening or plane stress condition causes certain deviation, the Rice-Johnson's solution in Fig. 3b provides the fundamental information of blunting with associated analytical strategy to connect near tip field solution (hole solution) with the surrounding small yield solution. This methodology will also be used for finding the electrical solution of blunted crack tip in this analysis.

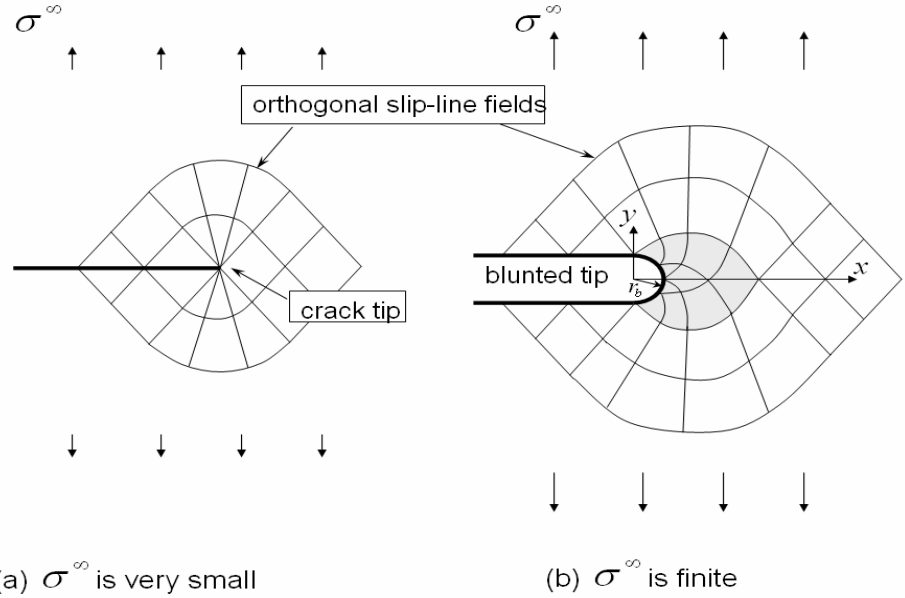

Fig. 3: The defect's geometry to be studied: (a) a crack with a mathematically sharp tip; its stress, strain and displacement fields are characterized by Prandtl slip-line field as plotted; (b) a crack with a blunted tip represented by the semi-circle of radius r_b and two parallel edges; where the shaded area in the front of the tip is the Rice-Johnson slip-line field [68] surrounded by the Prandtl field in (a).

3. Solutions of an Infinite Central-Cracked Conductive Plate under Constant Current

3.1 General Solution of Magnetic Field

Under the two-dimensional approximation and boundary conditions given in Section 2.3, Maxwell equations II and III in (2) can be satisfied by an "electric potential" φ:

$$\nabla^2\varphi = 0 \qquad \text{and} \qquad E_x = -\frac{\partial\varphi}{\partial x},\ E_y = -\frac{\partial\varphi}{\partial y} \tag{11}$$

Therefore, Maxwell equation IV of (2) yields:

$$\begin{bmatrix} \dfrac{\partial H_3}{\partial y} - \dfrac{\partial H_y}{\partial z_3} \\ -\dfrac{\partial H_3}{\partial x} + \dfrac{\partial H_x}{\partial z_3} \\ \dfrac{\partial H_x}{\partial y} - \dfrac{\partial H_y}{\partial x} \end{bmatrix} = \begin{bmatrix} J_x \\ J_y \\ J_3 \end{bmatrix} = \sigma^C \begin{bmatrix} E_x \\ E_y \\ E_3 \end{bmatrix} = \sigma^C \begin{bmatrix} -\dfrac{\partial\varphi}{\partial x} \\ -\dfrac{\partial\varphi}{\partial y} \\ 0 \end{bmatrix} \tag{12a}$$

Substituting (10a, 10e) or (10b, 10e) into (12a), its first two rows become:

$$-\frac{\partial\varphi}{\partial x} = \frac{\partial H_3}{\sigma^C \partial y}, \qquad \frac{\partial\varphi}{\partial y} = \frac{\partial H_3}{\sigma^C \partial x} \tag{12b}$$

In the complex plan z where z is defined by $z = x + iy$, Equation (12b) are the "Cauchy-Riemann" relations when φ and H_3 form an "analytical function" as following in the domain Ω where (12b) holds:

$$F(z) = -\varphi + i\frac{H_3}{\sigma^C} \tag{13}$$

So the relations (12b) and (13) imply:

$$\nabla^2 F(z) = 0 \quad \text{or} \quad \nabla^2\varphi = 0 \quad \text{and} \quad \nabla^2 H_3 = 0 \tag{14}$$

which can be stated as: for a plane stress or plane strain boundary-value problem governed by Maxwell equations (2) under the conditions (10a-10e), its electrical potential φ and the magnetic field H_3 associated with electrical current are the real and imaginary parts, respectively, of an analytical function defined by (13). Thus, when one of them is fixed, another can be solved through the Cauchy-Riemann condition (12b).

3.2 Solutions of Electrical Field with and without Breakdown

When the size of a defect, such as a crack, is much smaller than the size of a plane strain or plane stress conductor plate, the latter can be simplified as an infinitely large with remote

uniform electrical density field E^{∞}; which contains a central-located dielectric crack-shaped inclusion of length 2a without free charge on its surfaces. Also, under the steady-state approximation electrical currents stay unchanged during time evolution, which is true only when the time scale considered is very small.

Considering the two fundamental cases: electrical current bypasses the crack without or with electric-breakdown near the crack tips when E^{∞} is perpendicular to the crack, as illustrated by the Problem A and Problem B in Fig. 4a and 4b; respectively. For the case with breakdown, there is an arcing zone with the length Δ_b near the tip, in which a distributed current $\boldsymbol{J}_{breakdown}$ flows from one surface of the crack to its opposite.

The linearity of Maxwell's equations (2) allows the Problem *A* to be treated as the superposition of two sub-problems described in Fig 4a, denoted as problem *I* with solution $\{\varphi^I, H_3^I\}$ and problem *II* with $\{\varphi^{II}, H_3^{II}\}$, respectively. Similarly, the solution of Problem *B* is the superposition of problem A and another problem *III* with the solution $\{\varphi^{III}, H_3^{III}\}$ in Fig. 4b. Hence, instead of *A* and *B*, the issue becomes finding solutions for the relatively simplified cases *I*, *II,* and *III*. This solution strategy is borrowed from the BCSD (Bilby-Cottrell-Swinden-Dugdale) model in the dislocation analysis of crack [17, 18]. Introductions of the model, the general dislocation theory, and applications to crack problems, can be found, e.g. in [27,69].

Applying the complex function method introduced by Mushelishivili [21], the analytical solutions of the problems *I*, *II*, *III*, thus, *A* and *B*, have been obtained. The main results are listed below and a brief introduction of the derivations is given in Appendix I.

3.2.1 Problem I: Uniform Field

$$\varphi^I = yE^{\infty} + const, \qquad H_3^I = x\sigma^C E^{\infty} + const \tag{15}$$

3.2.2 Problem II: Crack Solution under Surface Current

$$-\varphi^{II}(z) + i\frac{H_3^{II}}{\sigma^C} = -iE^{\infty}\left(z - \sqrt{z^2 - a^2}\right) \tag{16}$$

3.2.3 Problem A: Crack Solution under Remote Uniform Current

Omitting the constant term, the superposition of (15) and (16) leads to:

$$-\varphi^A(z) + i\frac{H_3^A}{\sigma^C} = -iE^{\infty}\sqrt{z^2 - a^2} \qquad \text{and} \qquad E_x^A - iE_y^A = \frac{izE^{\infty}}{\sqrt{z^2 - a^2}} \tag{17}$$

Alternatively, the potential φ^A and electrical density field E^A can be respectively expressed in the following asymptotic forms in the polar coordinate system $\{r, \theta\}$ originated at a crack tip:

$$\varphi^A(r,\theta) \approx -\sin\left(\frac{\theta}{2}\right)E^{\infty}\sqrt{2ar} \qquad \text{when} \quad r \to 0 \tag{18a}$$

$$E_x^A(r,\theta)=E^\infty\sqrt{\frac{a}{2r}}\cos\frac{\theta}{2}\ ,\quad E_y^A(r,\theta)=E^\infty\sqrt{\frac{a}{2r}}\sin\frac{\theta}{2}\qquad \text{when}\quad r\to 0 \tag{18b}$$

Plotted in Fig. 5a is the local magnetic field, i.e. the imaginary part of (16). One sees that at the two ends of the crack H_3 reaches its peak values, $\pm E^\infty\sigma^C a$. Plotted in Fig. 5b are the contours of the electric potential of the problem *A*, i.e. the real part of (17). The corresponding amplitudes of electric currents in the *x* and *y* directions, respectively, are given in Fig. 5c and 5d. Both of them show singularity at the crack tip, i.e. $|x|=a, y=0$.

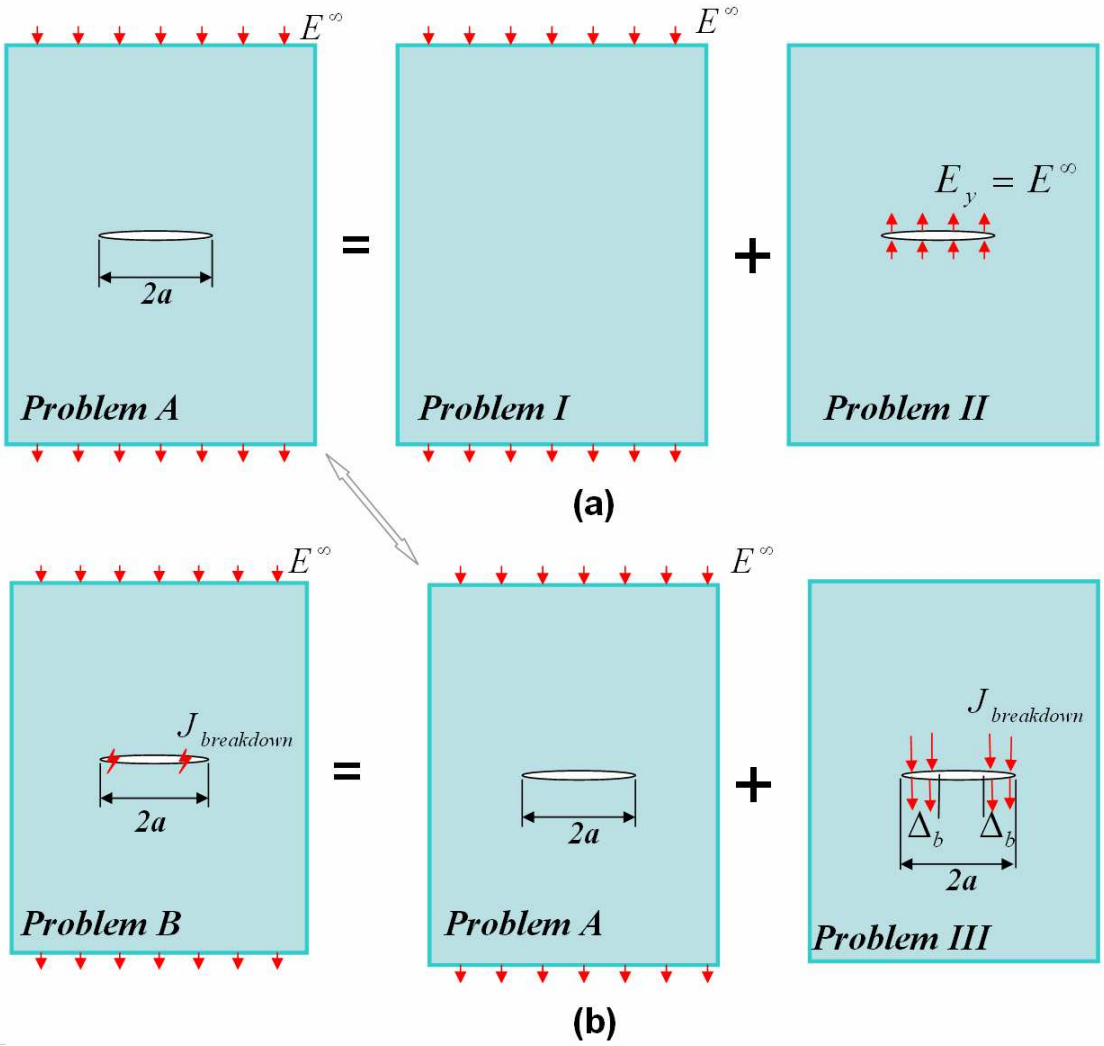

Fig. 4 Modified BSCD-Model – a strategy to obtain electrical field solutions: (a) Poblem *A*: which is the superposition of problem *I* and *II*; (b) Poblem *B*: which is the superposition of Poblem *A* and *III* , representing electric-breakdown within the small zone Δ_b near the crack tips.

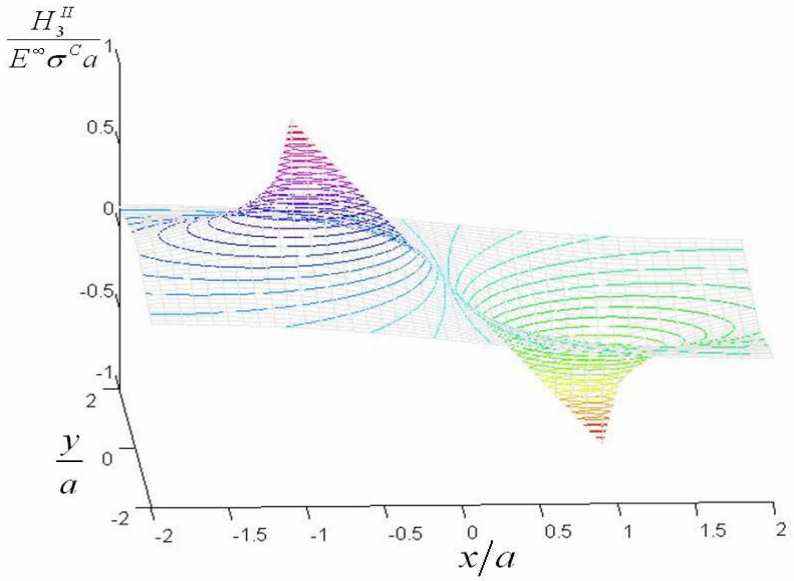

(a) Magnetic field H_3^{II} obtained from (16), the solution for the problem II in Fig. 4a

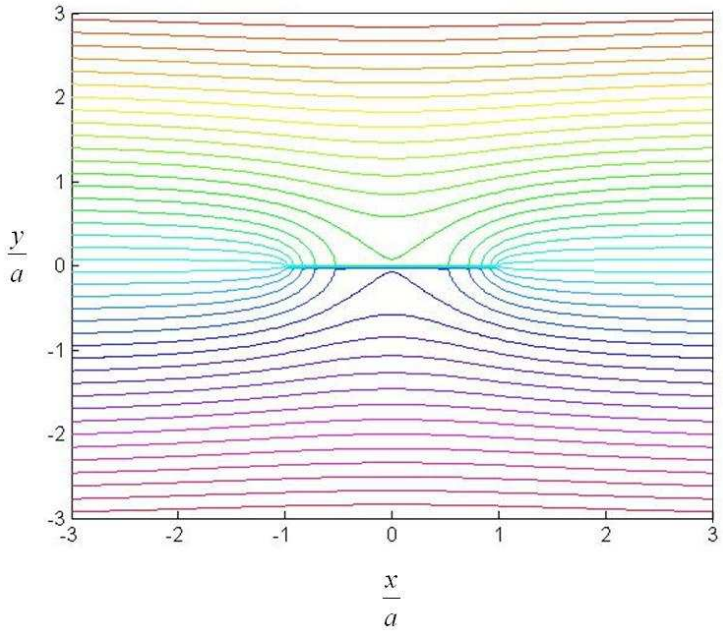

(b) The iso-valued contours of the total electric potential computed according to (17)

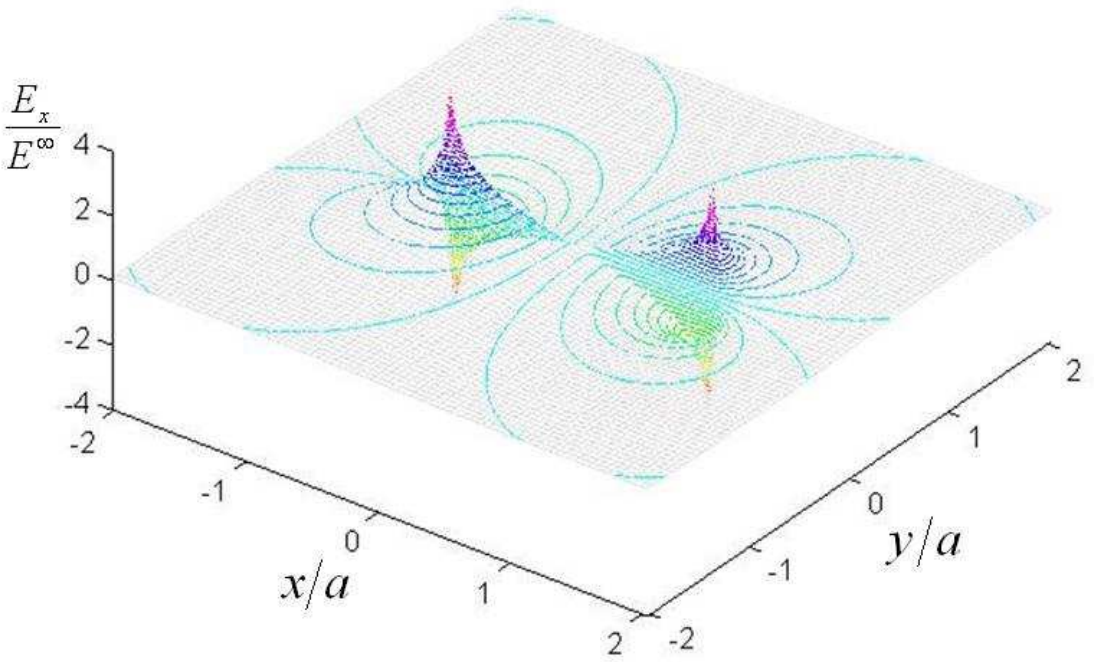

(c) Amplitude of the electric field in the x direction, which has singularities at $|x| = a, y = 0$

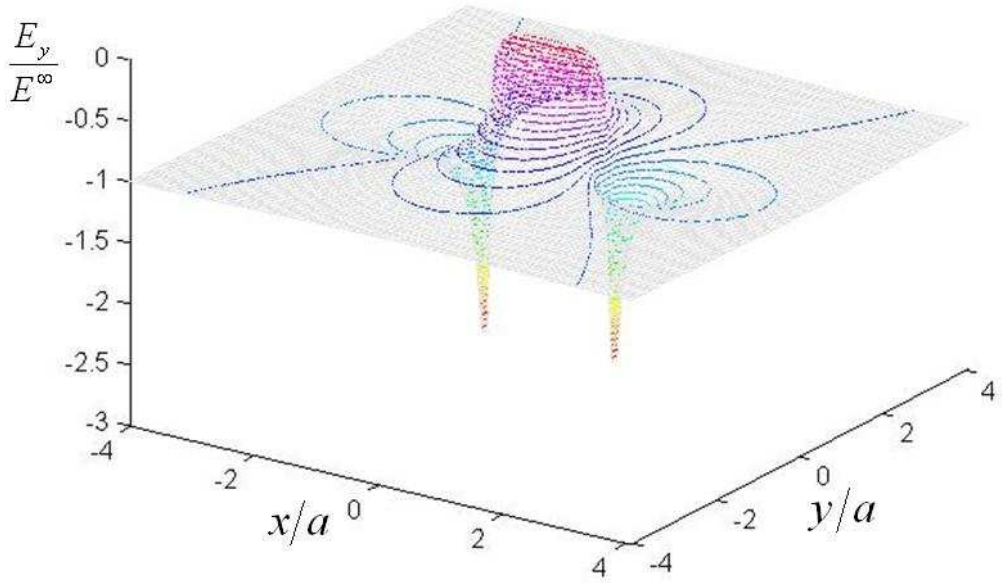

(d) Amplitude of the electric field in the y direction, which is zero along the line $|x| < a, y = 0$ but has a singularity at $|x| = a, y = 0$

Fig. 5 Solutions to the plane problems *I*, *II* and *A* in Fig. 4a.

3.2.4 Problems III and B:

Solution (18b) of Poblem *A* demostrates a "singular" current at the crack tip. In reality, when breakdown takes place, electrical current may penetrate the dielectric medium contained

by the crack, if this provides an easy path for electrical flow that removes the singular current field caused by the sharp tip. Mathematically, this breakdown current, $\boldsymbol{J}_{breakdown}$, can be counted as another electrical load on the crack surface, as described by the problem III in Fig. 4b. $\boldsymbol{J}_{breakdown}$ has the opposed direction as compared with the surface current load in the Problem II of Fig. 4a; so it ($\boldsymbol{J}_{breakdown}$) induces a singular electrical field but with opposite sign at the crack tip, which cancels the singularity in the solution (17, 18b). This trade-off provides a condition to determine the size of breakdown zone Δ_b.

As reported in [25, 26], experimental observations indicate that $\boldsymbol{J}_{breakdown}$ can be estimated by the following empirical relation:

$$\left|\boldsymbol{J}_{breakdown}\right| = \beta \frac{\Delta V_r}{\delta(r)} \qquad \beta = \tilde{\beta}\sigma^C \tag{19}$$

where $\tilde{\beta}$ is a dimensionless coefficient and $\tilde{\beta} \approx 100$ [25, 26]; $\delta(r)$ is the distance between two surfaces of the conductor. For the specimen in Figs.4a,b, $\delta(r)$ is the crack opening displacement between a pair of points on opposite crack surfaces with distance r to the tip, and ΔV_r is the difference in electrical potential between the two points. The solution of $\delta(r)$ will be given in the next section and ΔV_r is given by (18a). According to these solutions, the ratio $\Delta V_r / \delta(r)$ is constant when E^∞ is fixed. Then, applying the same procedure for Problem *II* in Fig. 4a, after superposition of the solutions, the following electrical potential and magnetic fields of the Problem *B* has been obtained:

$$\varphi + i\frac{H_3}{\sigma^C} = \frac{aB}{\sigma^C}\left\{C + i\pi z + \log\left[\frac{1 - \frac{zd}{a^2} - \sqrt{\left(\frac{d^2}{a^2}-1\right)\left(\frac{z^2}{a^2}-1\right)}}{1 + \frac{zd}{a^2} - \sqrt{\left(\frac{d^2}{a^2}-1\right)\left(\frac{z^2}{a^2}-1\right)}}\left(\frac{x-d}{x+d}\right)\right]\right\} \tag{20}$$

where C is a complex constant, and

$$B = \frac{2\beta G\sqrt{2}}{k_I v_\kappa \mu_M E^\infty \left(a\sigma^C\right)^2} \tag{21}$$

and Δ_b can be expressed by the following polynomial after a nonlinear regression:

$$\frac{\Delta_b}{a} = k_{B2}\hat{B}^2 + k_{B3}\hat{B}^3 + k_{B4}\hat{B}^4, \qquad \hat{B} = \frac{\sigma^C E^\infty}{B} \tag{22}$$

where

$$k_{B2} = 0.1250984\,, \qquad k_{B3} = -0.00040127\,, \qquad k_{B4} = 0.003033 \qquad (23)$$

Plotted in Fig. 6a is the potential drop between the two opposite crack surfaces according to (20) while in Fig. 6b is the regressive solution of Δ_b expressed by (22).

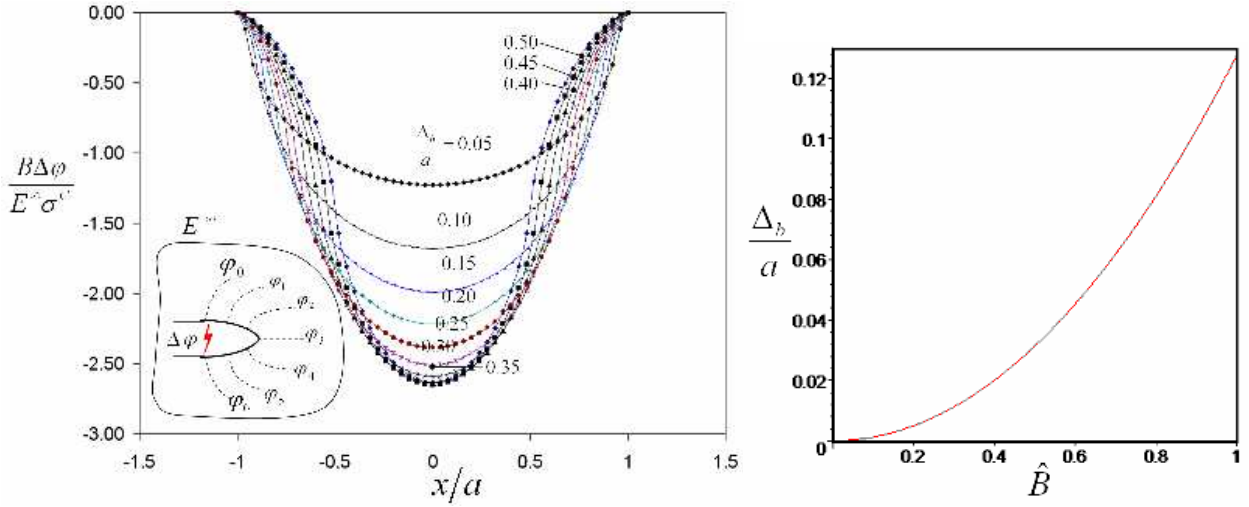

Fig. 6 (a) the potential drop between the two opposite crack surfaces according to (20), expressed as the dimensionless number $\dfrac{E^{\infty}\sigma^{C}}{B}$; (b) Regressive solution of arcing zone size Δ_b

3.2.5 Problem C: Solution of Circle Hole

As illustrated by Fig. 3, a long crack with blunted tip can be treated as a notch with two parallel wedges and ended by a semi-circle hole of diameter r_b. The near field solution for a circle hole in a very large plate has the same structure as that in the local area ahead of a semi-circled notch tip; where "very large" means that the dimensions of the plate, i.e., its width and height, are much greater than the radius of the hole. Therefore, this subsection studies the solution of a circle-shaped dielectric inclusion in an infinite conductor plate, see Fig. 7a. Although this is another extreme case of ellipsoid inclusion when its short and long axes become equal, this condition leads to an infinite large radius according to the classical ellipsoid solution [20].

As a straight-forward application of the procedure applied in the previous subsections, the corresponding electrical potential $\varphi^{C}(z)$ and magnetic field $H_3^{C}(z)$ have been obtained:

$$-\varphi^{C}(z) + i\frac{H_3^{C}(z)}{\sigma^{C}} - = \frac{1}{2}\left(\frac{\partial U(z)}{\partial x} - i\frac{\partial U(z)}{\partial y}\right) + \phi(z) \qquad (24)$$

where

$$\phi = \frac{E^{\infty}}{4}\left(z + \frac{2r_b{}^2}{z}\right), \quad U(z) = \frac{1}{2}\left[z\phi(z) + \bar{z}\bar{\phi}(z)\right] \tag{24a}$$

Plotted in Figs. 7b and 7c are the contours of $\varphi^C(z)$ and $H_3^C(z)$, respectively. The potential drop between two ends of the hole in the current direction, denoted as $\Delta V_{\delta 0}$, yields:

$$\Delta V_{\delta 0} = 4E^{\infty} r_b \tag{25}$$

Remark: (24) and (25) can be verified by substituting $z = x + iy$, $\bar{z} = x - iy$ into (24a) then (24), which leads to:

$$\varphi = -\frac{E^{\infty}}{2}\left[x + \frac{x^3 + y^2 x + 2xr_b}{x^2 + y^2}\right]$$

$$E_x = \frac{E^{\infty}}{2}\left[1 + \frac{3x^2 + y^2 + 2r_b}{x^2 + y^2} - \frac{2\left(x^3 + y^2 x + 2xr_b\right)x}{\left(x^2 + y^2\right)^2}\right]$$

$$E_y = E^{\infty}\left[\frac{xy}{x^2 + y^2} - \frac{\left(x^3 + y^2 x + 2xr_b\right)y}{\left(x^2 + y^2\right)^2}\right]$$

where the x coordinate is in the vertical direction of Fig. 7a.

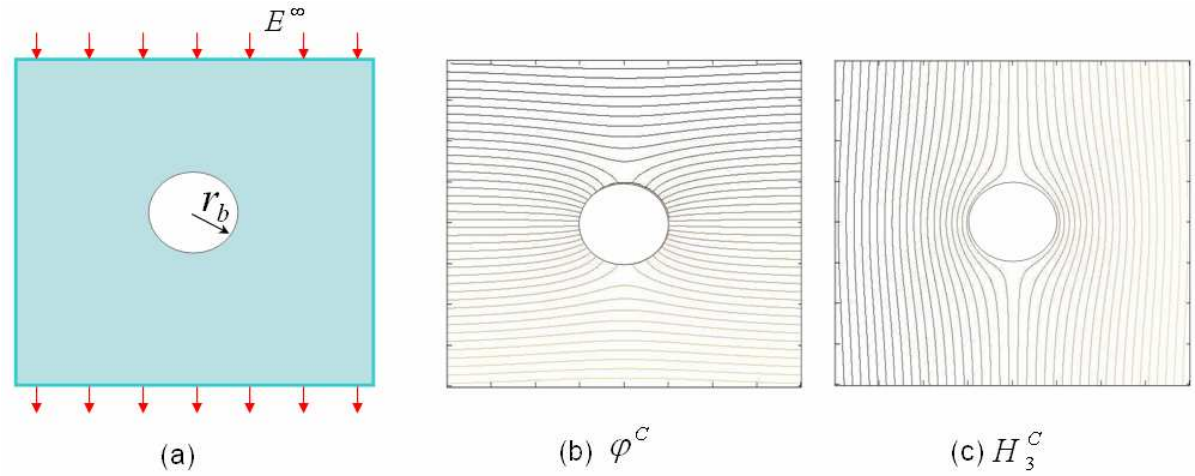

Fig. 7 (a): Problem C: an infinite large conductor plate containing a circle hole under uniform electrical field E^{∞} at remote; (b) and (c): contours of the electrical potential and magnetic field in the area around the hole.

3.3 Solution of Stress Intensity Factor Caused by Lorentz Force

In the following analysis, symbol "*d*" represents unit thickness for both plane stress and plane strain cases. Under this convention electric current and its density have the same magnitude but with an implicit difference (square of unit length) in dimension. Hence, for simplification, symbol "***J***" can stand for either electric current or electric current density upon the context of applications.

Recall the equilibrium equation (1): when the magnetic field perpendicular to the plate, i.e. H_3, is taken into account, the first term on the right hand side is a high order small quantity that can be left out; the corresponding Lorentz force is determined by the second term, presented as a distributed load p_R per unit area "*dxdy*" in $\{x, y\}$ plane:

$$p_R(z) = \rho_e(\boldsymbol{v}_q \times \boldsymbol{B}) = (\boldsymbol{J} \times \boldsymbol{H})\mu_M = -\sigma^C \mu_M (E_x + iE_y) \cdot (H_3) \tag{26}$$

where μ_M is the magnetic permeability. According to (15) the amplitude of the magnetic field H_3^I is proportional to the *x*-coordinate so it is relatively weak in the area around the crack; whereas at remote, since E_x vanishes, H_3^I produces the Lorentz force along the direction parallel to the crack. Therefore the following analysis focuses on the magnetic field solved in problem II: H_3^{II}.

For a two-dimensional cracked panel like those in Fig. 4 under a mechanical load, e.g. (26), the corresponding stress field near the crack tip can be expressed by the following asymptotic formulation in the polar coordinate system $\{r, \theta\}$ originated at the crack tip [22]:

$$\sigma_{ij} = \frac{1}{\sqrt{2\pi r}} \left[K_I \phi_{Iij}(\theta) + K_{II} \phi_{IIij}(\theta) \right] \tag{27}$$

where subscripts "*I*" and "*II*" refer to mode I and II crack tip fields, corresponding to tension and shear load, respectively; the detailed expressions of the angular factors $\phi_{Iij}(\theta), \phi_{IIij}(\theta)$ can be found in [22]. Then, according to the procedure introduced in [23, 24], the corresponding stress-intensity factors in (27) are:

$$\begin{aligned} K_I - iK_{II} &= \frac{1}{2(1+\kappa)\sqrt{a\pi}} \int_{-\infty}^{\infty} \int_{-\infty}^{\infty} (p_R(z)\Phi_1(z) + \overline{p}_R(z)\Phi_2(z)) dxdy \\ &= \frac{\mu_M (a\sigma^C E^\infty)^2 \sqrt{\pi a}}{2(\kappa+1)} \{k_I - ik_{II}\} \end{aligned} \tag{28}$$

and

$$k_I = \frac{3-\kappa}{2}, \quad k_{II} = 0 \tag{29}$$

where $\kappa = (3-\nu)/(1+\nu)$ for plane-stress and $\kappa = 3-4\nu$ for plane-strain. The double infinite integrals in (28) are solved analytically by the conformal mapping $z = \frac{a}{2}\left(\varsigma + \frac{1}{\varsigma}\right)$ that transforms the infinitely large conductor plate in Fig.4 into the circle with a unit radius centered at the origin of the ς plane while transforms the crack with length 2*a* into the rest area of the plane, as illustrated in Fig. 8. Details of this procedure can be found in [21].

For mechanical boundary value problem, stress field (27) and stress intensity factors (28) determines the displacement field through (6), the corresponding crack opening displacement (COD) along the wedges near a mathematically sharp crack tip can also be expressed asymptotically in the polar coordinate system originated at the tip:

$$\delta_{COD}(r) \approx v_\kappa k_I \sqrt{ar}\,\frac{\mu_M \left(a\sigma^C E^\infty\right)^2}{G}, \quad v_\kappa = \frac{2(1-\nu)}{(\kappa+1)\sqrt{2\pi}} \qquad \text{for} \quad r \to 0 \tag{30a}$$

For a blunted crack illustrated in Figs 3b, the corresponding COD can be expressed as:

$$\delta(r_{eff}) = \delta_t + \delta_{COD}(r_{eff}) \tag{30b}$$

the first term on the right hand side of (30b), δ_t, is the crack tip opening displacement (CTOD) defined as below:

$$\delta_t = \delta_b + b_0 \sigma_Y J_{\text{int}} \tag{30c}$$

where b_0 equals *1* for plane stress and *2* for plane strain [22]; σ_Y is material's yield strength; J_{int} is the J-integral [28]:

$$J_{\text{int}} = \frac{K_I^2}{E'} \qquad \text{and} \qquad E' = \begin{cases} E & \text{plane stress} \\ \dfrac{E}{1-\nu} & \text{plane strain} \end{cases} \tag{30d}$$

where K_I is given by (28) and *E* is Young's module.

The second term on the right hand side of (30b) is the COD defined by (30a) but *r* is replaced by r_{eff} that is a function of *x*, the horizontal coordinate in Fig. 3b, and is determined by the continuing condition of electrical potential between the circle hole solution (25) and the crack tip solution (18a) at the intersection between the circle tip profile and straight wedge of the crack in Fig. 3b:

$$4E^\infty r_b = 2E^\infty \sqrt{2a r_{eff}(x)} \qquad \text{at} \qquad x = 0 \tag{30e}$$

which leads to:

$$r_{eff} = -x + \frac{2(r_b)^2}{a} \qquad \text{for} \quad x \le 0 \tag{30f}$$

For a crack tip without blunting: $r_{eff} = r$.

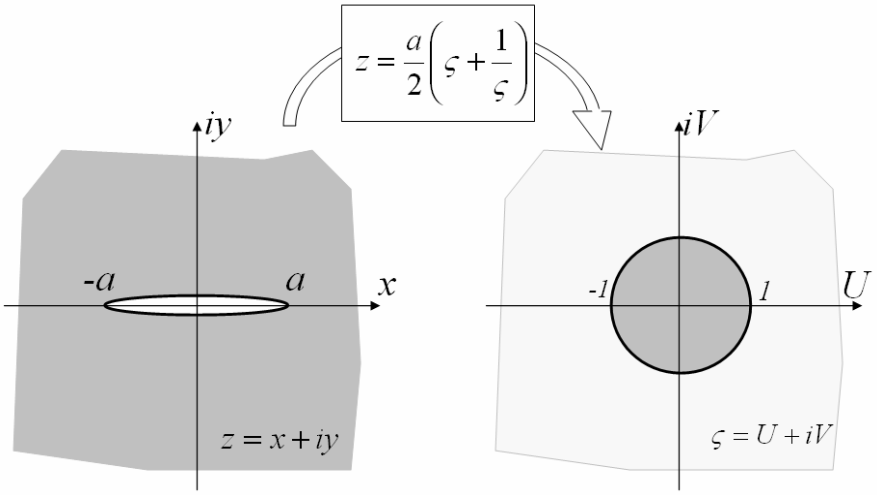

Fig. 8 Conformal mapping to obtain integration (28), which transforms the z plane on the left into the area surrounded by the circle with a unit radius in the ς plane on the right, while the area contained by the crack into the rest area of the ς plane, see [21].

4. The Two Competing Failure Mechanisms: Breakdown and Melting

4.1 A Circuit Model for the Two Mechanisms

We study the condition of breakdown based on the solutions (15-18a,b) and (20). Considering the material point pair (A_0, A_6) plotted on the left hand side of Fig. 9, which sits on the opposite surfaces near a crack tip with a potential difference: $\Delta V_{06} = \varphi_0 - \varphi_6$ according to (18a) and Fig. 5(b). This potential difference may drive electric current flowing through two possible ways: bypassing around the crack tip or breaking the dielectrical barrier between A_0 and A_6 by arcing. These two competing mechanisms can be simplified as the capacitance-resistance circuit model for a given current illustrated on the right-hand side of Fig. 9. When current goes through the resistance unit that represents the crack tip, the corresponding energy dissipation can be estimated by:

$$\Delta\Psi_{bypass} = R\int_{\Gamma} \left|\boldsymbol{J}_{bypass}\right|^2 d\Gamma \approx 2R_C \int_0^{r_6} \left|\boldsymbol{J}_{bypass}\right|^2 dr \tag{31}$$

where $\boldsymbol{J}_{bypass}$ is the current along the path bypassing crack tip; R is electric resistance; r_6 is the distance to crack tip.

On other hand, when breakdown takes place within the area at the distance equal and less than r_6, the energy dispassion is

$$\Delta\Psi_{breakdown} = \int_{r_i}^{r_6}\int_{0}^{\Delta V_r} \nabla\varphi \cdot \boldsymbol{J}_{breakdown} d\varphi dr \approx \int_{r_i}^{r_6} \Delta V_r \cdot \left|\boldsymbol{J}_{breakdown}\right| dr \tag{32}$$

where ΔV_r is the potential difference at the point on crack surface with the distance r to the tip; $\boldsymbol{J}_{breakdown}$ is the breakdown current; r_i is the distance that no breakdown when $r < r_i$.

Thus, the condition for the occurrence of electric-breakdown can be written as below:

$$\Delta\Psi_{breakdown} \le \Delta\Psi_{bypass} \tag{33}$$

According to the experimental results, e.g. [5, 6, 25, 26], breakdown is an instant, complex process by which the voltage induced E field ionizes dielectric medium through exciting electrons to the orbits with higher energy level which may break the chemical bond to release more energy and make the dielectric medium be a "conductor". Once this process occurs, the corresponding breakdown current reaches its peak value, empirically expressed by (19), within a short time interval through arcing, followed by subsequent geometric change of the conductor due to melting. Under the aforementioned short time interval and "steady-state" approximations, by substituting (18a) and (30) into (19):

$$\left|\boldsymbol{J}_{breakdown}\right| \approx \frac{2\beta G\sqrt{2}}{k_I v_\kappa \mu_M E^\infty \left(a\sigma^C\right)^2}, \tag{34}$$

which reveals that the amplitude of the breakdown current is approximately constant in the arcing zone.

According to (18b) the bypass current density yields:

$$\left|\boldsymbol{J}_{bypass}\right| \approx \sigma^C E^\infty \sqrt{\frac{2a}{r}} \tag{35}$$

Substituting (34) into (32) and (35) into (31), respectively; and let $r_i = 0$ in (32), one obtains:

$$\Delta\Psi_{breakdown} = \frac{16\beta G\Delta_b^{\frac{3}{2}}\sqrt{a}d}{3k_I v_\kappa \mu_M \left(a\sigma^C\right)^2} \tag{36}$$

and

$$\Delta\Psi_{bypass} = 2k_L adR\left(\sigma^C E^\infty\right)^2 \left[\log(r)\right]_{r_{tip}}^{\Delta_b}, \qquad r_{tip} \to 0 \tag{37}$$

where d is the thickness of the specimen; Δ_b is given by (22); k_L is a constant with the dimension of length when $\boldsymbol{J}_{bypass}$ is current density.

Substituting (22) into (36) and omitting the terms in (22) with the order higher than 2, an alternative expression of the total energy dispassion at electric-breakdown is obtained:

$$\Psi_{breakdown} = \left(\sigma^C\right)^{\frac{5}{2}} \left(E^{\infty} a \sqrt{k_{B2}}\right)^3 \left(\frac{8\sqrt{2}}{9} \frac{k_I v_\kappa \mu_M}{\beta G}\right)^{\frac{1}{2}} d \tag{38}$$

When the electrical potential and current in (32), respectively, are replaced by displacement and stress relation, one can find that the resulted equation is identical to the *J*-integral derived in the BCSD model in continuum fracture mechanics [28]. Considering breakdown is an onset point that material losses its capacity against crack growth, $\Psi_{breakdown}$ in (32) and (38) represents the "fracture toughness" under this condition.

On contrast, equation (37) suggests the current bypasses induced energy dissipation proportional to $-\log\left|r_{tip}\right|$ whereas for a mathematically sharp crack tip r_{tip} approaches zero. This implies that an electric-breakdown is a natural phenomenon, which can be inevitable under certain circumstance, e.g. a sharp crack without tip blunting. Consequently, the conditions for blunting and the corresponding energy dissipation become the objects to be studied hereafter.

Experimental observation [5] indicates that breakdown takes place only when the intensity of applied electric field reaches a certain critical value. This leads to another question: what happens at a crack tip when the electric field is below the critical value? There are at least three possibilities: (i) the crack tip in the tested specimen being initially "blunted"; (ii) the tip is initially "sharp" but the stress intensity factors (28) induced by Lorentz' force cause development of plastic zone in the form of Rice-Johnson-Prandtl's field (Fig. 3b); according to (30c,d):

$$\delta_t = \left(\frac{k_I \mu_M}{2(\kappa+1)}\right)^2 \left(\sigma^C E^{\infty}\right)^4 \frac{b_0 \pi a^5 \sigma_Y}{E'} \tag{39}$$

so in (37) $r_{tip} \approx \delta_t$ which removes the singularity; however, since δ_t is proportional to $\left(\sigma_Y \mu_M^2\right)/E$, its absolute value is very small and the integral (37) can still be considerable high; (iii) the last possibility is that the energy dissipation associated with the singular electric field (18b) is transformed into thermal vibrations with localized high temperature field, which "melts" the sharp crack tip into a blunted "hole". Since (31) and (37) are very simplified estimates, the following subsection develops a more precise solution of the temperature field around a crack tip.

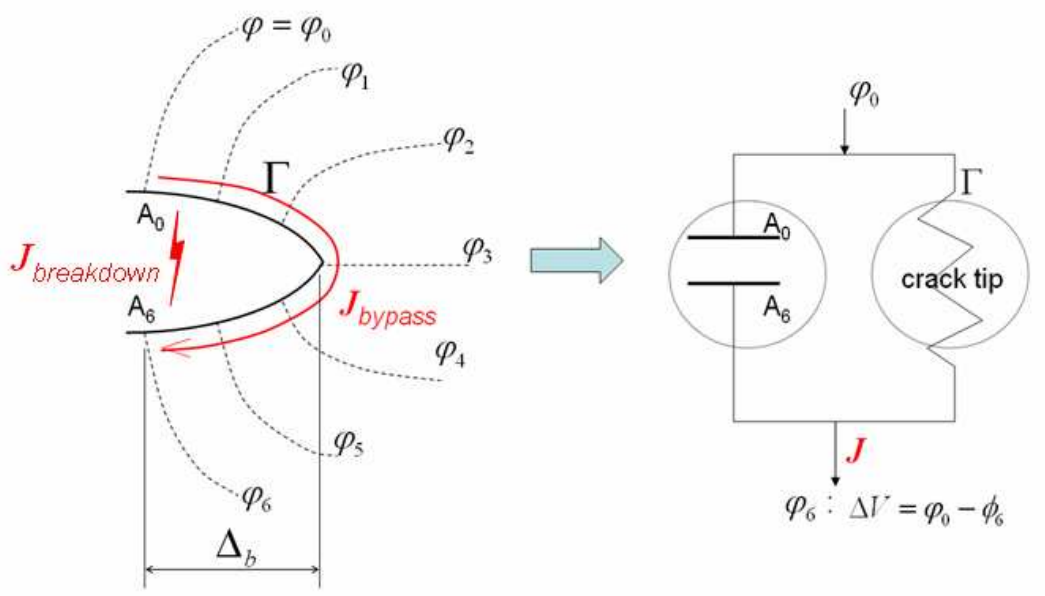

Fig. 9 Models for breakdown analysis: (a) A circle model that represents two competing mechanisms around a crack tip: the current breaks through the capacitance unit A_0A_6 or goes around the crack tip resistance

4.2 Temperature Field Solution - Thermal Dissipation Analysis

The asymptotic behavior of the temperature field near a crack tip before breakdown is investigated, presuming the field to be governed by the heat-conduction equation (7), which is consistent with the previous stated "steady-state" approximation within small time interval; so all corresponding solutions are "rate" independent. Also it is assume the heat conduction coefficient and electrical resistivity are constants. Then the electrical field solutions of cracks obtained in previous section are applicable except in the very small area just ahead blunted tip. According to (17) the energy dissipation per unit area; which defines the heat source density ρ_H in (7), yields:

$$\rho_H = R_C |\boldsymbol{J}|^2 = \sigma^C \left(E^\infty\right)^2 \frac{iz\bar{z}}{\sqrt{\left(z^2 - a^2\right)\left(\bar{z}^2 - a^2\right)}} \tag{40}$$

where $\boldsymbol{J}$ is the current density; R_C is the resistivity, and $R_C = 1/\sigma^C$.

By substituting the asymptotic expression (18b) into (40) then into (7), the governing equation of heat conduction in the polar coordinate system originated at the crack tip reads:

$$\nabla^2 T = \frac{a}{r}\frac{\left(E^\infty\right)^2 \sigma^C}{2k_H} + o\left(r^{-1}\right) \qquad \text{for} \qquad r << a \tag{41}$$

which leads to the following temperature field solution:

$$T = \frac{\left(E^{\infty}\right)^2 \sigma^C}{2k_H}\left(\frac{r}{a} - C_1\left(\log\left(\frac{r}{a}\right) + i\theta\right) - C_2\left(\log\left(\frac{r}{a}\right) - i\theta\right) + C_3\right) \qquad (42)$$

where the C_1, C_2, and C_3 are real constants. Removing the imaginary part of (42) leads to a constraint to its coefficients: $C_1 = C_2 = C$ which cancels the terms with angle θ.

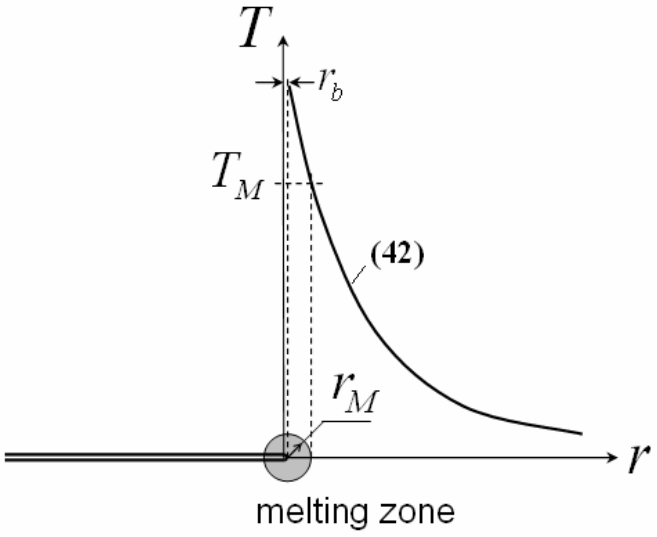

Fig. 10 An "asymptotic" two-phase model for the temperature field near a crack tip;

For most metal-based conductors, melting is the process that crystals loss their long-range periodic orders. According to the analysis in [29, 30], at the temperature just above melting point (T_M), liquid metals usually present as amorphous structure (one-dimensional quasi-crystal) which segregate into particles in the size 2-10nms with weak connection between each other. A direct consequence is that the material loss stiffness against deformation. Any mechanical load, e.g. Lorentz' force (26,27), drives a viscostic-like flow in the melting zone and cause the tip blunting, as described by the Rice-Johnson-Prandtl field in Fig. 3b. Thus, a two-phase model of a solid crack panel with crack tip melting zone, as illustrated in Fig. 10, is introduced to describe these phenomena approximately. At the border between the solid conductor and the melting zone the temperature must be the solid-liquid phase transformation temperature, denoted as T_M.

Obviously melting is a dynamic process. Once electrical load applies to a cracked conductor, the material near the sharp crack tip starts to melt due to the high amplitude of current and associated energy dissipation concentration. This concentration causes continuing expansion of the melting zone until it reaches a relatively stable state after the electrical resistance induced dissipation balances the extra energy exhausted by the capacity heat to warm up the material and latent heat of phase transformation. This process can be described by the following two stages,

characterized by the quantity ∂_Q, the heat flow that passes through the solid-liquid boundary at $r = r_M$:

Stage I: warm up in the time interval $0 \le t \le \Delta t$, the initial material temperature is T_0:

$$\int_0^{\Delta t}\int_0^{2\pi} \partial_Q r d\theta dt = \int_0^{\Delta t}\int_0^{2\pi}\int_{r_b}^{r_M} \left[R_C |\boldsymbol{J}|^2 - \rho_m k_D \left[C_f + c_{sp}(T - T_0)\right]\right] r dr d\theta dt \tag{43a}$$

where r_M is moving; at $r = r_M$:

$$\partial_Q = -\left.\frac{\partial T}{\partial r}\right|_{r=r_M}, \qquad T = T_M, \qquad R_C \left|\tilde{\boldsymbol{J}}_M\right|^2 = \rho_m k_D \left[C_f + c_{sp}(T_M - T_0)\right] \tag{43b}$$

In (43a,b) $\tilde{\boldsymbol{J}}_M$ is the current density at the solid-liquid border; C_f is the solid conductor's fusion enthalpy per unit mass, i.e. the energy absorbed during solid-liquid phase transformation; c_{sp} is the heat capacity of solid conductor; ρ_m is mass density and k_D is a unit constant but with the dimension of 1/*t* (1/second). Thus, product $C_f \rho_m$ is the latent heat per unit volume

Stage II: steady state ($t \ge \Delta t$):

$$\int_0^{2\pi} \partial_Q r d\theta = \int_0^{2\pi}\int_{r_b}^{r_M} \left[R_C |\boldsymbol{J}|^2\right] r dr d\theta \tag{44a}$$

where r_M is constant; at $r = r_M$:

$$\partial_Q = -\left.\frac{\partial T}{\partial r}\right|_{r=r_M}, \qquad T = T_M, \qquad R_C \left|\tilde{\boldsymbol{J}}_M\right|^2 = \rho_m k_D \left[C_f + c_{sp}(T_M - T_0)\right] \tag{44b}$$

Under the aforementioned approximations, in stage II the temperature fields of both the melting zone and solid phase obey (42). Using the first two relations of (44b) to fix the constants *C* and C_3 in (42), it becomes:

$$T = T_M + \frac{\left(E^\infty\right)^2 \sigma^C a}{2k_H}\left[\frac{r}{a} - \frac{r_M}{a} - \frac{r_M}{a}\log\left(\frac{r}{r_M}\right)\right] - \partial_Q \log\left(\frac{r}{r_M}\right) \qquad a >> r \ge r_b \tag{44c}$$

where r_b is given by (39).

Also, according to (18b) at $r = r_M$:

$$|\boldsymbol{J}|^2 = \left|\tilde{\boldsymbol{J}}_M\right|^2 = \frac{\left(E^\infty \sigma^C\right)^2}{2}\frac{a}{r_M}, \tag{45}$$

For simplification, the case that $c_{sp}\Delta T << C_f$ at $T = T_M$ is considered, so the second term in the last equation of (44b) can be omitted. By combining it with (45) an estimate of r_M, the size of the melting zone, is obtained:

$$r_M = \frac{\left(E^\infty\right)^2 \sigma^C}{2\rho_m k_D \left(C_f + c_{sp}\Delta T\right)} a \approx \frac{\left(E^\infty\right)^2 \sigma^C a}{2\rho_m k_D C_f} \tag{46a}$$

which leads to a threshold of remote electrical field intensity for melting:

$$E^\infty_{melting} = \sqrt{\frac{2r_b \rho_m k_D C_f}{\sigma^C a}} \tag{46b}$$

It indicates that for a mathematically sharp crack tip ($r_b = 0$) melting will take place once E^∞ is nonzero but it will have a finite value if $r_b > 0$. It will be a straightforward to obtain r_M and $E^\infty_{melting}$ when $c_{sp}\Delta T$ is also taken into account.

Therefore, the energy dissipation that creates the melting zone yields

$$\Delta\Psi_{melt} = \int_0^{\Delta t} dR_C \int_0^{2\pi} \int_{r_b}^{r_M} |\boldsymbol{J}|^2 r dr d\theta = \Delta t R_C d\pi \left(\sigma^C E^\infty\right)^2 \left[r_M - r_b\right] \tag{47}$$

where r_M is given by (46). It is reasonable to further assume that the energy consumption in the melting zone is much greater than that in the solid phase due to latent heat; then after taking Δt be unit time the equation (37) can be rewritten in the form as:

$$\Delta\Psi_{bypass} \approx \Delta\Psi_{melt} \approx \pi\, r_M\, dR_C \left(\sigma^C E^\infty\right)^2 \tag{48}$$

5. The Threshold of Applied Electric Field Intensity for Breakdown and Melting

The crack problems solved in the previous sections were discussed in the framework of macroscopic mean-field theories. Solution (46) indicates that a melting zone will occur at a sharp crack tip once E^∞ is nonzero, whereby the following questions are raised:

- What is the length scale that defines the applicability of the obtained solutions, since the governing equations (1-8) are under "mean field" approximation and the macro scale-sized cracks are considered?
- How to justify the effects of small-sized defects at atomic scale?

Focused on these questions, in this section we study the interaction between atomistic-sized impurities and electronic transportation under the framework of semiclassical theory of conduction in metals, establishing quantitative linkage from submicro and quantum physics to the derived mean field theory-based solutions, so as to obtain engineering applicable criteria for the two competing failure mechanisms: breakdown and melting. The introduction of the semiclassical theory can be found, e.g. in [16, 31]. The discussions about fracture toughness and the length scale in mechanical analysis can be found in [4, 28, 32-36].

5.1 Microscale defects and A Length Parameter that Bridges Solutions from Different Scales

5.1.1 About the Ohm's law

It is well-known that micro and nano scaled defects, such as dislocations and impurities, have significant effects on material's mechanical properties. This subsection studies their effects on electron transportation process and material's conductivity. According to the framework of the "semiclassical theory of conduction in metal" [16]: in electric current flow all electrons stay in a fixed, not fully occupied, conduct band without inter-band transportation. Electric resistance is essentially the subsequent result of collisions between electron and electron, electron and lattice imperfection, and, electron and nuclei thermal vibration (phonon). For ideal conductive metal there will be no such collisions. The average time between two collisions defines "relaxation time", denoted as "τ_R". Electric current density is an average of the product between the velocity of electron defined in $\boldsymbol{k}$ space, $\boldsymbol{v}(\boldsymbol{k})$, and the deviation of charge distribution function from equilibrium state $\Delta \boldsymbol{g}$:

$$j = -e\int \frac{d\boldsymbol{k}}{4\pi^3}\boldsymbol{v}(\boldsymbol{k})\Delta \boldsymbol{g} \tag{49}$$

where

$$\Delta g = -e\boldsymbol{E}\cdot\boldsymbol{v}(\boldsymbol{k})\tau_R(\varepsilon_n)\frac{\partial f(\varepsilon_n(\boldsymbol{k}))}{\partial \varepsilon_n} \tag{50}$$

where $\varepsilon_n(\boldsymbol{k})$ is the energy associated with electron e at n^{th} band, which is a function of the moment vector $\boldsymbol{k}$ in reciprocal space, and $f(\varepsilon)$ is the Fermi-Dirac function of energy distribution. Hence, electric conductivity σ^C is a tensor that sums the contribution from all n conducting bands:

$$\boldsymbol{\sigma}^C = e^2\sum_n \int \frac{d\boldsymbol{k}}{4\pi^3\hbar}\tau(\varepsilon_n)\boldsymbol{v}(\boldsymbol{k})\boldsymbol{v}(\boldsymbol{k})\frac{\partial f(\varepsilon_n(\boldsymbol{k}))}{\partial \varepsilon_n} \tag{51}$$

When Hall's effect is omitted, only one conduct band is taken into account and isotropic approximation applies, (51) degenerated to the classical expression in Drude's theory:

$$\sigma^C = \frac{ne^2\tau(\varepsilon_F)}{m} \tag{52}$$

where n and m denote the density and mass of electrons, respectively; ε_F is Fermi's energy.

It is well-known that, by assuming the same relaxation time for both electric flow and heat conduction, the "mean free path" l_m, i.e. the average distance that a conduction electron travels between two collisions, is the product of Fermi velocity, v_F, and τ_R:

$$l_m = v_F \tau_R \tag{53}$$

Obviously the "mean free path" l_m in (53) characterizes the space that restricts the motion of each single electron, which can be used as the smallest size of "cell" to define the average behavior of electrons in mean field theory if τ_R is known. By omitting the electron-electron interaction, since it becomes significant only under very low temperature, the effective relaxation time can be expressed as the geometrical average of that for electron-phonon interaction, denoted as τ_{e-p}, and that for electron-imperfection interaction, τ_{e-i}. According to Matthiessen's rule:

$$\frac{1}{\tau_R} = \frac{1}{\tau_{e-p}} + \frac{1}{\tau_{e-i}} \tag{54}$$

The Block's T^5 law indicates that τ_{e-p} is proportional to $\left(\frac{\Theta_D}{T}\right)^3$ if temperature T (Kervin) is much smaller than Derby temperature Θ_D. When T is the same order or larger than Θ_D the following relation is suggested in appendix J of [31] for electron-phonon interaction:

$$\frac{1}{\tau_{e-p}} = \frac{K^2 m^* k_F k_B T}{\pi c_S \rho_m \hbar^3} \tag{55}$$

where K, k_B, and c_S denote volumetric Young's module, Boltzmen's constant and the speed of light, respectively; k_F is the radius of Fermi surface in reciprocal space, and m^* is the equivalent mass of electron.

5.1.2. Electron-Imperities Interaction

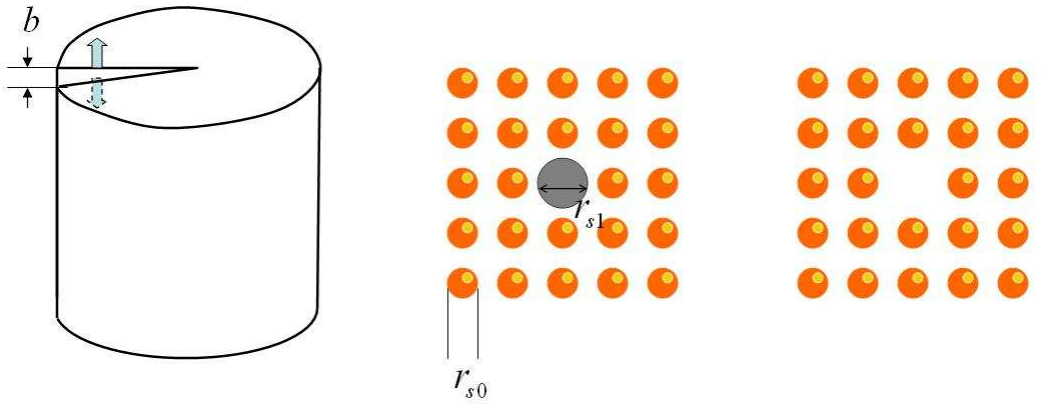

Fig. 11 Three impurities studied which causes electric resistance: (a) screw dislocation; (b) misfitted solution atoms; (c) empties.

Hence, a particularly interests is given to electron-impurities interaction in this study. Three kinds of common impurities are taken into account: screw dislocation core, empty and solution atoms, as illustrated in Fig. 11. According to the first-order perturbation theory, e.g. [31, 37, 38] and recently [39, 40], a crystal lattice elastic strain causes change of the effective potential in the Hamiltonian to the electron wave functions, which yields:

$$\Delta U(\boldsymbol{r}) = \nabla \boldsymbol{r} : \partial \boldsymbol{U}$$

where $\partial \boldsymbol{U}$ refers to a parameter associated with "deformed potential", which is an integration of lattice distortion-induced strain energy over certain length scales. By the approximation of "dilute distribution" for an impurity that sits at the origin, $\partial \boldsymbol{U}$ is taken as the derivative of deformation energy with respect to deformation gradient; then for linear elastic small lattice deformation $\Delta U(\boldsymbol{r})$ can be approximated by the total deformation energy caused by an impurity.

Hence, for an electron at the band with index *n*, according to the semi-classical theory the relaxation time can be expressed as below:

$$\frac{\boldsymbol{g}(\boldsymbol{k}) - \boldsymbol{g}_0(\boldsymbol{k})}{\tau_{e-i}(\boldsymbol{k})} = \int \frac{n_{imp}}{(2\pi)^3} W(\boldsymbol{k}, \tilde{\boldsymbol{k}}) \{\boldsymbol{g}(\boldsymbol{k})(1 - \boldsymbol{g}(\tilde{\boldsymbol{k}})) - \boldsymbol{g}(\tilde{\boldsymbol{k}})(1 - \boldsymbol{g}(\boldsymbol{k}))\} d\tilde{\boldsymbol{k}} \tag{56}$$

where n_{imp} is the number of impurities per unit volume; $\boldsymbol{g}(\boldsymbol{k})$ is distribution function of electron with current flow and $\boldsymbol{g}_0(\boldsymbol{k})$ is that at equilibrium condition; $W(\boldsymbol{k}, \tilde{\boldsymbol{k}})$ is the scattering function:

$$W(\boldsymbol{k}, \tilde{\boldsymbol{k}}) = \frac{2\pi}{\hbar} \delta(\varepsilon(\tilde{\boldsymbol{k}}) - \varepsilon(\boldsymbol{k})) \left| \langle \boldsymbol{k} | \Delta U | \tilde{\boldsymbol{k}} \rangle \right|^2 \tag{56a}$$

where $\hbar$ is Planck's constant, and,

$$\left\langle \boldsymbol{k}\left|\Delta U\right|\tilde{\boldsymbol{k}}\right\rangle = \int d\boldsymbol{r}\overline{\psi}_{n\tilde{k}}(\boldsymbol{r})\Delta U(\boldsymbol{r})\psi_{nk}(\boldsymbol{r}) \tag{56b}$$

where $\psi_{nk}(\boldsymbol{r})$ is normalized plane wave function corresponding to momentum $\boldsymbol{k}$ with band index n and (56b) is the element matrix, e.g. defined in [38]. As introduced in [41], varies methods can be used to calculate $\Delta U(\boldsymbol{r})$. In this study the continuum lattice elastic theory is employed. Then, according to the analysis, e.g. [69, 27], $\Delta U(\boldsymbol{r})$ for line screw dislocation is available. Also, the Eshelby's eigen-strain method [42] provides the way to obtain the approximated solutions of $\Delta U(\boldsymbol{r})$ for diluted empty and misfit atom. In general,

$$\Delta U_i(\boldsymbol{r}) = \frac{A_i}{r^{n_i}}, \qquad \frac{b}{2} \le r \le r^i_{cut-off} \tag{57}$$

where the subscription $i = 1,2,3$ stands for screw dislocations, misfit solution atom, and single empty site, respectively; and $n_1 = 1$, $n_2 = n_3 = 3$; the values of the coefficient A_i are listed in Table 1. The potential well defined by (57) are essentially applicable up to infinite. For the convenience of analysis, the cut-off radius $r^i_{cut-off}$ is defined by

$$\Delta U_i\left(r^i_{cut-off}\right) = \alpha_{cut-off}\Delta U_i\left(\frac{b}{2}\right) \tag{57a}$$

where $\alpha_{cut-off}$ is an *ad hoc* coefficient that must be much smaller than unit; since $\Delta U_i(\boldsymbol{r})$ is fast degenerated function when $\boldsymbol{r}$ increases and its contribution can be omitted when $r > r^i_{cut-off}$. In order to be consistent with the convention in statistic analysis, in this study $\alpha_{cut-off} = 0.03$ is taken.

Table 1: Coefficients of (57)

	A_i
screw dislocation	$-\frac{Gb^4}{2\pi^2}$
misfit solution atom	$-\frac{19\pi^2 Gb^6(1-M_b)^2}{12\left(1+\frac{2}{3}M_G\right)}$
empty site	$-\frac{G\pi^2 b^6}{105}$

where

$$M_G = \frac{G_2}{G}, \qquad M_b = \frac{b_2}{b}$$

where G_2 and b_2 are the bulk Young's module and Burger's vector for the solution atom.

In this paper the following additional assumptions have been adopted for obtaining the analytical solutions of the relaxation time:

(i) Sphere Fermi surface with the radius $k_F = k_{FR}$; consequently:

$$\int \frac{n_{imp}\, g(\boldsymbol{k})}{(2\pi)^3} W(\boldsymbol{k}, \tilde{\boldsymbol{k}}_\perp) d\tilde{\boldsymbol{k}} = 0 \qquad (57)$$

where $\tilde{\boldsymbol{k}}_\perp$ is the component of $\tilde{\boldsymbol{k}}$ perpendicular to $\boldsymbol{k}$, see Fig. 12.

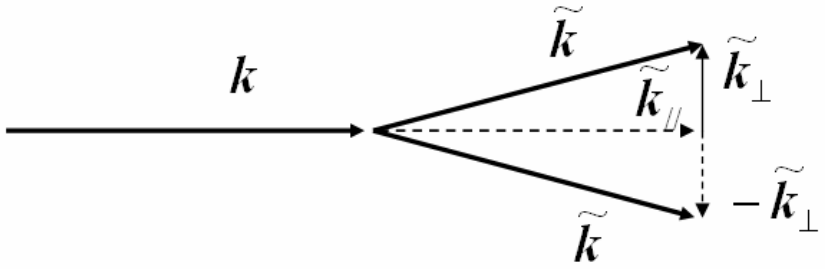

Fig. 12 Eq.(57) implies the equal-probability for the collisions $\tilde{\boldsymbol{k}}_\perp$ and $-\tilde{\boldsymbol{k}}_\perp$.

(ii) Quasi-isotropic charge distribution [16]:

$$\boldsymbol{g}(\boldsymbol{k}) = \boldsymbol{g}_0(\boldsymbol{k}) + \boldsymbol{a}(\boldsymbol{k}) \cdot \boldsymbol{k} \qquad (58)$$

(iii) Generalized Matthiessen's rule: additive summation for three different impurities for the scattering function in (57):

$$W(\boldsymbol{k}, \tilde{\boldsymbol{k}}) = \frac{2\pi}{\hbar} \delta(\varepsilon(\tilde{\boldsymbol{k}}) - \varepsilon(\boldsymbol{k})) \left| \sum_{j=1}^{3} n_{imp}^{j} \left| \langle \boldsymbol{k} | \Delta U_j | \tilde{\boldsymbol{k}} \rangle \right| \right| \qquad (59)$$

(iv) Only the closed neighbor atoms to the impurity site are taken into account, so:

$$\langle \boldsymbol{k} | U | \tilde{\boldsymbol{k}} \rangle = \sum \int \overline{\psi}_{n\tilde{k}} (\boldsymbol{r} - \boldsymbol{r}_{\tilde{R}}) \Delta U(\boldsymbol{r}) \psi_{nk} (\boldsymbol{r} - \boldsymbol{r}_R) d\boldsymbol{r}, \quad |\boldsymbol{r}_{\tilde{R}}| < r_{cut-off}, \quad |\boldsymbol{r}_R| < r_{cut-off}$$

(v) The probability of Umklapp scattering is ignorable as compared with other mechanisms.

(vi) Under the assumptions mentioned above, the following relation is applicable

$$d\varepsilon(\boldsymbol{k}) \approx \frac{\hbar^2}{m_e^2}\boldsymbol{k}\cdot d\boldsymbol{k} \tag{60}$$

, so there will be no difference between mass and equivalent mass of electron;
in (60), m_e=9.11$\cdot 10^{-31}$(kg); $\hbar$: Planck's constant $\hbar$=6.6262$\cdot 10^{-34}$ ($j\cdot t$).

(vii) Classical expression of Fermi velocity

$$v_F \approx \left(\frac{\hbar}{m_e}\right)k_F \qquad \text{(meter/second)} \tag{61}$$

The values of the material's constants appear in the equations in this subsection are listed in Table II. Applying the approximations and omitting high order small quantities, the dominant terms in the solutions of (56) are:

$$\frac{1}{\tau_{electron-dislo}(\boldsymbol{k}_F)} = \frac{256\log(b/2)mG^2b^8r_{cut-off}^3}{59049\pi^2\hbar^3k_F^7a_0{}^8}\left(\frac{r_{cut-off}^3}{d_i^3}\right)\left[1+O\left(\frac{1}{(k_f d_i)^2}\right)\right] \tag{62a}$$

$$\frac{1}{\tau_{electron-atom}(\boldsymbol{k}_F)} = \frac{18496m(A_2)^2r_{cut-off}^3}{43046721\hbar^3k_F^3a_0{}^{10}}\left(\frac{r_{cut-off}^3}{d_i^3}\right)\left[1+O\left(\frac{1}{(k_f d_i)^2}\right)\right] \tag{62b}$$

$$\frac{1}{\tau_{electron-empty}(\boldsymbol{k}_F)} = \frac{18496m(A_3)^2r_{cut-off}^3}{43046721\hbar^3k_F^3a_0{}^{10}}\left(\frac{r_{cut-off}^3}{d_i^3}\right)\left[1+O\left(\frac{1}{(k_f d_i)^2}\right)\right] \tag{62c}$$

where a_0: Bohr's radius, a_0= 0.5292(A); d_i is the average distance between impurities and the following relation has been applied:

$$n_{imp} = \frac{1}{d_i^3} \tag{63}$$

Remark: For the N-ion crystal with the impurities in the form of vacancy(empty), the thermodynamic estimate of the number of vacant site is [16]:

$$n_{vac} = N\exp(-\alpha_0\varepsilon_f)$$

where α_0 is a constant. More advanced discussions can be found, e.g. in [50-53].

By substituting (62a,b,c) into (53), one finds that for all three kinds of impurities the mean free path yields:

$$l_m \propto b\frac{d_i^3}{r_{cut-off}^3} \tag{64}$$

For example, after substituting the material's constants of iron in Table II into (62a) and (53), one obtains:

$$\frac{1}{\tau_{electron-dislo}} \approx \frac{\alpha_\tau}{4\pi^2} d_i^{-3}, \qquad \alpha_\tau = 1.08\cdot 10^{-8}\,(1/\mathrm{m}^3) \tag{65a}$$

and

$$l_m \approx \alpha_l \pi^2 d_i^3, \qquad \alpha_l = 7.25\cdot 10^{16}\,(1/\mathrm{m}^2) \tag{65b}$$

When the average distance between screw dislocation lines is 50nm, i.e. $d = 5\cdot 10^{-8} m$, then

$$l_m \approx 633nm \tag{66}$$

i.e. l_m is around a micron, which is a reasonable length scale to define the lower bound of mean field theory. However, a paradox exists since (65b) implies that the mean free path can be infinite large when the density of impurities is zero; the corresponding conductivity also becomes infinite. Since impurities always exist in real metal crystals and most metal conductors are polycrystalline, grain boundary can be considered as an upper bound of mean free path. Hence, this study suggests the following estimate:

$$L_m = \min\{l_m, d_m\}, \qquad d_m: \text{average size of grains} \tag{67}$$

to be the length scale that defines the availability of mean field theory. Replacing the r_M in (46) by L_m, we obtain an estimate of the intensity of applied electric field to initiate "melting" at a sharp crack tip:

$$E_{melt}^{\infty} = \sqrt{\frac{2L_m \rho_m C_f k_D}{a\sigma^C}} \tag{68}$$

Table II: Material's constants[16] applied in the equations (56-63)

	Ag	Cu	Fe	Al
G(GPa)	75.8	110	193	62
$k_F(\frac{1}{A})$	1.2	1.36	1.714	1.745
$v_F(\frac{10^6 m}{s})$	1.3925	1.573	1.981	2.029

where kg: kilogram mass; m: meter; t: second; j: joul; A: angstrom.

5.2 Paschen Law and Threshold of Applied Electrical Load

The "semi-classical theory" applied in the previous subsection fails when interband transportation of electrons, i.e. breakdown between electron orbits, takes place, which may results in formation of new interatomic bands or ionization of atoms when electrons become free, resulted in the release of chemical bonding energy. A macroscopic breakdown as shown in Fig. 1 usually is the subsequent result of the applied voltage-induced ionization of the dielectric medium filled in the crack. This complex process can be phenomenologically described by the Paschen law [43]. This empirical law indicates that the occurrence of electric-breakdown is determined by the gap width between two electrodes and the voltage difference inbetween; where the latter can be expressed by a function (generally not linear) of the product of the pressure, p, of the dielectric medium and the gap, δ:

$$\Delta V_{breakdown} = f(\delta, p) \tag{69}$$

For gas, the pressure should be replaced by the gas density. For the problem addressed in Figs.1-4, the opposite crack surfaces work as two electrodes with the potential difference given by (18a), so the gap width δ is the crack opening displacement defined by (30a,b). When δ is much smaller than a millimeter, recent study [44] suggested the following expression:

$$\Delta V_{breakdown} = g\delta \tag{70}$$

where g is a constant in the order of 10^2(V/μ) when δ is in the unit of micron (μ).

As an electrical field is always accompanied with magnetic field that causes Lorentz' force and corresponding crack opening, a question is whether this crack opening displacement plays can be used in (70) since electrical current and magnetic wave travel with the speed of light whereas propagation of deformation is limited by the speed of elastic wave; so a breakdown and subsequent material failure may occur before crack opens. Experiments indicate that the process of electrical breakdown usually lasts longer than millisecond; the time scale for this process is strongly dependent upon environment temperature but generally is enough for an elastic deformation. This class of phenomena is generally termed "time-dependent dielectric breakdown"(TDDB)[70,71]. Thus, in this study, it is presumed that the Lorentz' force induced crack opening defined by (30a,b) occurs before breakdown induced material's failure.

As plotted in Fig. 5b, the voltage difference has the maximum value at the center of a crack while degenerates to zero at a sharp crack tip where the separation is also zero. Thus, as illustrated in Fig. 13 for a conductor crack or a contact between two conductors there are at least three breakdown patterns, depending upon the distribution of voltage difference and profiles of crack opening displacement and/or contact surfaces. In the follows the solutions of electrical potential (17, 18a) and COD given by (30a-e) are used to identify which pattern will happen in reality and to find the corresponding critical value of E^{∞} at breakdown; the latter defines the threshold of electrical load, denoted as $E^{\infty}_{breakdown}$.

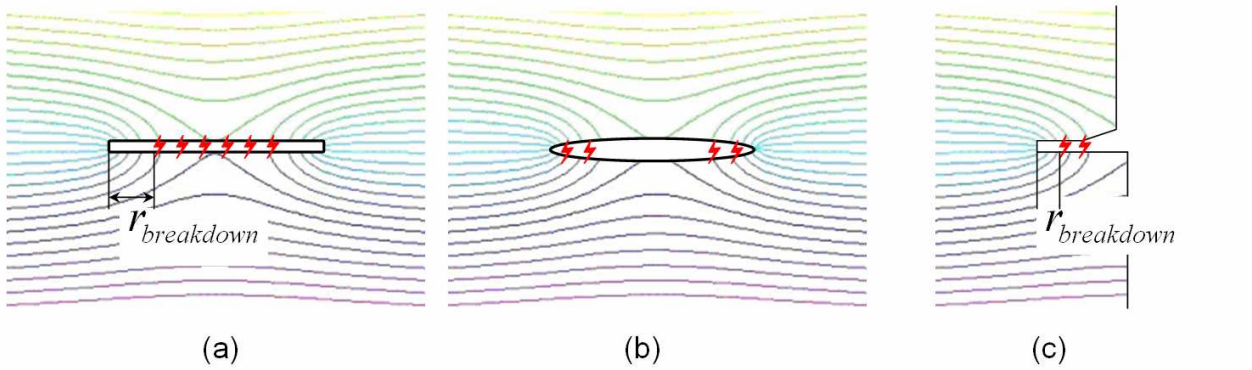

Fig. 13 Three patterns of electric-breakdown: (a) with a distance to crack tip; (b) at crack tip; (c) within a localized area away from the tip; where the contours are electrical potential. Occurrence of actual pattern depends upon crack opening profile and electrical potential distribution, which are the functions of crack geometry, level of applied load, material's electrical, magnetic and mechanical properties.

Starting at the configuration illustrated in Figs 3b, the δ in (70) is given by (30a,b):

$$\delta(r_{eff}) = \delta_t + \delta_{COD}(r_{eff}) \tag{30b}$$

and

$$\delta_{COD}(r_{eff}) = \frac{4(E^{\infty})^2\sqrt{r_{ref}a}}{A_0} \quad \text{and} \quad A_0 = \frac{2G}{v_\kappa k_I \mu_M (a\sigma^C)^2} \tag{30a}$$

According to (18a) and (25), the electrical potential drop between the two opposite surfaces yields:

$$\Delta V = E^{\infty}\left(4r_b + 2\sqrt{2r_{ref}a}\right) \tag{71}$$

When the crack tip initial radius is much greater than the deformation-induced radius increase, i.e., omitting the second term of (30c); then, $\delta_t \approx r_b$. By substitute (30b) into the right hand side of (70) while (71) into its left hand side, the $E^{\infty}_{breakdown}$ is the root of E^{∞} for the resulted equation:

$$E^{\infty}\left(4r_b + 2\sqrt{2r_{ref}a}\right) - \left(\delta_b + \frac{4(E^{\infty})^2\sqrt{r_{ref}a}}{A_0}\right)g = 0 \tag{72}$$

For a crack with sharp tip: $r_b = 0$ and $r_{eff} = r$, the non-trivial solution of (72) is:

$$E^{\infty}_{breakdown} = \frac{A_0}{g\sqrt{2}} \tag{73}$$

Therefore, under this situation the breakdown will take place once $E^{\infty} \geq E^{\infty}_{breakdown}$, starting at crack tip, as illustrated in the Fig. 13(b).

For $r_b > 0$, the non-trivial solution of (72) yields:

$$E^{\infty}_{breakdown} = \frac{A_0}{g2\sqrt{2}}\left[1 + r_b\sqrt{\frac{2}{ar_{eff}}} + \sqrt{1 - \frac{2g^2 r_b}{A_0\sqrt{ar_{eff}}} + \frac{2r_b}{\sqrt{ar_{eff}}}\left(\sqrt{2} + \frac{r_b}{\sqrt{ar_{eff}}}\right)}\right] \quad (74)$$

By substituting (30f), i.e. $r_{eff} = -x + \frac{2(r_b)^2}{a}$, into (74), $E^{\infty}_{breakdown}$ is the solution satisfying the following condition where *x* is defined in Fig.3b:

$$\frac{\partial E^{\infty}_{breakdown}}{\partial x} = 0, \qquad \frac{\partial^2 E^{\infty}_{breakdown}}{\partial x^2} > 0 \quad (75a)$$

Since the first two terms of (74) are monotonic to r_{eff}, instead of solving the first relation of (75), the minimum of (74) can be obtained by the minimum of its third term:

$$\frac{\partial E_I}{\partial x} = 0 \quad \text{and} \quad E_I = 1 - \frac{2g^2 r_b}{A_0\sqrt{ar_{eff}}} + \frac{2r_b}{\sqrt{ar_{eff}}}\left(\sqrt{2} + \frac{r_b}{\sqrt{ar_{eff}}}\right) \quad (75b)$$

which leads to

$$x = \frac{r_b^2}{a}\frac{A_1\left(A_1 - 2\sqrt{2}\right)}{\left(A_1 - \sqrt{2}\right)^2} \quad \text{and} \quad A_1 = \frac{g^2}{A_0} = \frac{v_\kappa k_I \mu_M \left(a\sigma^C g\right)^2}{2G} \quad (76)$$

By varying the material's constant A_1 there will be two cases: (i) $A_1 \geq 2\sqrt{2}$ so $x \geq 0$; breakdown occurs in the circle-shaped crack tip, corresponding to the case illustrated in Fig. 13(b); (ii) $A_1 < 2\sqrt{2}$ so $x < 0$; breakdown occurs in the area with a distance $r_{breakdown}$ to the crack tip, as illustrated in Fig. 13(a); the $r_{breakdown}$ yields:

$$r_{breakdown} = r_b + \frac{r_b^2}{a}\frac{A_1\left(A_1 - 2\sqrt{2}\right)}{\left(A_1 - \sqrt{2}\right)^2} \quad (77)$$

5.3 Breakdown or Melting ? A Derived Material's Constant to Identify the Governing Mechanism

Relationship (68) gives E^{∞}_{melt} at onset of crack tip melting whereas (73,74) predicts the threshold at breakdown. For engineering material there will be three different cases: (i) $E^{\infty}_{breakdown} < E^{\infty}_{melt}$: breakdown dominates the material's failure process when applied electrical load $E^{\infty} \le E^{\infty}_{melt}$ and $E^{\infty} \ge E^{\infty}_{breakdown}$; (ii) $E^{\infty}_{breakdown} > E^{\infty}_{melt}$: crack tip melting zone-induced thermosoftening and subsequent crack propagation may present once $E^{\infty}_{melt} \le E^{\infty}$; (ii) $E^{\infty}_{breakdown} = E^{\infty}_{melt}$: both mechanisms may occur simultaneously.

Further more a practical question is: when an electrical load $E^{\infty} \ge \max\left(E^{\infty}_{breakdown}, E^{\infty}_{melt}\right)$ is imposed to a conductor with crack, which process, melting or breakdown, will govern the material's failure? In order to identify the dominant mechanism under this situation for an engineering material, a "comparison factor" is introduced as below:

$$D_p = \frac{\Delta\Psi_{bypass}}{\Delta\Psi_{breakdown}} \tag{78}$$

where $\Psi_{breakdown}$ is defined by (38) and $\Delta\Psi_{bypass}$ by (48) in which the r_M is defined by (46); also $E^{\infty} = E^{\infty}_{breakdown}$ defined by (73) is applied in this relation. Table III lists the values of the dimensionless constant coefficients presented in (38, 46, 48, 73).

Table III:

v (Possion's Ratio)	κ	v_k	k_I	k_D	k_{B2}
0.3	$(3-v)/(1+v)$	0.1815	$(3-\kappa)/2$	1	0.12509

Obviously, when D_P defined by (78) is greater than unit, electrical breakdown dominates whereas the melting mechanisms takes over when $D_P < 1$, which provides a hint for the design of materials or devices with desirable dominant mechanism. This is because, in contact systems made of conductors, the mechanical, electrical, and temperature fields near the edges between two contact surfaces essentially have the same structures as that near a crack tip [48, 49, 55-57].

Listed in Table IV are the material constants of four common used conducting metals and the corresponding values of D_P. In the second row from the bottom one finds $D_P > 1$ for the three nonferric metals (Ag, Cu, Al) as well as for the iron at the low ferric end; whereas $D_P < 1$ for the iron at high ferric end. This is because higher permeability μ_M results in larger Lorentz's force through equ.(20), which leads to larger crack opening displacement as indicated by (30) and, subsequently, requires higher voltage at breakdown according to Paschen's law (70). Hence, one may conclude that for a cracked specimen made of low ferric metals, electric-breakdown may occur easily, triggered by existing defects like cracks. On contrast, for the cracked specimen made of ferric metals with high magnetic permeability, or the specimen is under an external mechanical force and magnetic field, which causes higher "k_I" in (28), crack tip melting and subsequent thermal induced materials softening may become the more favorite mechanisms.

It should be pointed out that D_P in the third row from the bottom of Table IV is obtained by "k_I" based on the local field solution (16) for the problem *II* in Fig.4a. When the global field, i.e. the problem A or B in Fig. 4 is taken into account, or an external mechanical force is imposed, the corresponding value of k_I will be different. However, the resulted change is only quantitatively and basic trend maintains. In order to demonstrate this effect, D_P for $k_I = 300$ and $k_I = 500$, respectively, are also calculated and listed in the last two rows of Table IV.

On other hand, an occurrence of electric-breakdown also depends upon the properties of the dielectric medium confined by the crack surfaces of the conductor. This fact is represented by the coefficient $\tilde{g}$ in (78) which is a function of the parameters β in (19) and g in Paschen's law (70). These two parameters were obtained empirically through experimental studies in [25, 44]. When environment changes, for examples, the humidity of air is high or the crack contains different kinds of gas, the values of β and g can be quite different, which may have remarkable effects on the amplitude of D_P.

Table IV: Material's constants (at room temperature) and the comparison factor D_P

	Ag	Cu	Fe	Al
G(GPa)	75.8	110	193	62
$\rho_M\ (\frac{kg}{m^3})$	10500	8960	7870	2700
$\sigma^C\ (\frac{10^6}{\Omega \cdot m})$	63	59.6	9.93	37.8
$\beta\ (\frac{10^8}{\Omega \cdot m})$	63	59.6	9.93	37.8
$g(\frac{10^8 V}{m})$	1.1	1.1	1.1	1.1
$\mu_M\ (\frac{10^{-7} H}{m})$	4π	4π	300-50000	4π
$H_f\ (\frac{j \cdot 10^5}{kg})$	1.048	2.087	2.437	3.97
$C_P\ (\frac{j \cdot 10^2}{kgK})$	2.35	3.85	4.49	8.97
D_P $k_I = \frac{3-\kappa}{2}(equ.24)$ plane stress	$1.79 \cdot 10^4$	$2.02 \cdot 10^4$	$8.01 \cdot 10^3$ ~ 3.72	$3.71 \cdot 10^4$
D_P $\left(k_I = 3 * 10^2\right)$ plane stress	1.08	1.21	$0.483 \sim 2.24 \cdot 10^{-4}$	2.24
D_P				

$(k_I = 5*10^2)$ plane stress	0.5018	0.566	$0.225 \sim 1.04 \cdot 10^{-4}$	1.042

kg: kilogram mass; m: meter; V: voltage; t: second, j: joul; H: Henry; crack length "a" = 0.02m; the values of β and g are collected from [25, 44]; all material's constants are in SI unit.

Remark 1: Ferric metals, such Fe, Ni, and Co, present spontaneous macroscopic magnetic ordering at room temperature. Such magnetic ordering can be changed through crystal structure distortion or addition alloying [10]. For example, pure iron crystal can be either face centered cubic (fcc) or body centered cubic (bcc). The former is a metastable antiferromagnetic structure at ground state, which has ordered spin-polarization pair at atomic scale but does not present spontaneous magnetic ordering at macroscale. The bcc is a stable ferromagnetic phase at ground state. The Neel temperature of fcc iron is about 67K[45], characterizing the loss of microscale magnetic ordering of antiferromagnetic phase. The Curie temperature of Fe is about 1043K, by which the bcc iron losses its macroscale magnetic ordering. When temperature rises, fcc structure will become a stable phase, instead of bcc. Crystal structural changes [60] or tiny alloys additions, such carbon[46], may stabilize fcc structure of iron so alter its magnetic properties. Plotted in the Figures of Appendix II are the first-principle computations reported in [46] for the fcc-bcc transformation, their magnetic moment, and the transition temperature under different pressures. These aforementioned research reports explain various reasons to cause diversified values of μ_M for Fe appear in Table IV. .

Remark 2: The concept introduced by (78), i.e. to identify dominant mechanism by comparing energy dissipations, is inspired by the methodology introduced in [47], by which the emission of dislocations in metal is determined by the path with lower energy barrier between sliding and brittle cleavage.

6. Conclusions

This paper studies the mechanisms of crack-induced failure in conducting metals, focused on the interaction among magneto-electrical load, thermal and mechanical responses and the associated two competing processes: crack tip melting and electric-breakdown. Three issues are emphasized: (i) strategies and technique to obtain theoretical solution; (ii) field solutions of several key-cracked configurations governed by Maxwell's equation, momentum conservation and heat conduction equation; (iii) physics insight: identify the effects of materials and defect geometries on electric-breakdown, melting, and subsequent crack growth, so as to provide engineering applicable criteria for material's selection and design of system under electrical loading.

Regarding the first issue, it has been proven that for two-dimensional conductors and dielectric solids, the solution to quasi-static Maxwell's equations can be expressed as an analytical function in a complex plane in general. The real part of this analytical function equals the electric potential with minus sign and the imaginary part is the product of a constant and the magnetic field corresponding to the electrical current field solution, when conductivity is constant and Hall effect is omitted since no external magnetic field applies.

Three groups of analytical solutions have been obtained, which are (i) Exact solutions of electric field, magnetic field, and Lorentz's force field for a central cracked infinite plane under a constant electric current at remote without electric-breakdown at crack tip (Problem A in Fig. 4a); (ii) Sharing the analytical technique in dislocation analysis, exact solution of the electric field with breakdown has been obtained based on a proposed "modified BCSD model" (Problem B in Fig. 4b); and (iii) a solution of the crack tip temperature field based on a proposed melting zone model.

The theoretical solutions reveal that the singularity in electric field at sharp crack tip leads to a concentration of energy dissipation, which results in localized high temperature, electric-breakdown and melting of the material in close vicinity of the tip. When there is no external magnetic field and mechanical load, the Lorentz force induced by the magnetic field associated with electric current may cause remarkable stress intensity factor, which drives crack opening and possible subsequent propagation since either electric-breakdown or energy dissipation-induced melting will significantly reduce material's capacity against crack propagation.

In order to quantitatively identify the governing mechanism that triggers crack growth, a "capacitance-resistance" circuit (CRC) model is proposed to highlight the physical process at crack tip under electrical load (Fig. 9). Enhanced by this model, a "comparison factor" D_p defined by equation (78) is proposed to distinguish which mechanisms, breakdown or melting, will become dominant around a defect such as a crack tip. This "comparison factor" suggests that low magnetic permeability or low conductivity makes electric-breakdown to be a favorite mechanism; whereas external mechanical force or the magnetic and electrical loads that causes larger crack opening displacement elevate the required break-down voltage so crack tip melting and thermally induced softening may dominate subsequent material failure.

When electric-breakdown is dominant, this analysis indicates that there three patterns of breakdown regarding the location where it happens, depending upon crack tip geometry, material's properties, and the level of applied mechanical load. The condition for crack tip breakdown, the distance to crack when breakdown occurs away from a crack tip, and the threshold of applied electrical load have been obtained analytically, listed in equations (73-77). For a mathematically sharp crack, the energy dissipation associated with breakdown has also been obtained in equation (38), which is mathematically identical to the J-integral in fracture mechanics. So it represents the "fracture toughness" of a material against breakdown induced crack growth.

Based on semiclassical theory of conductors the elastic collisions between electron and impurities have also been studied. Solutions for three kinds of impurities: screw dislocation, solution misfited atom and an empty, have been obtained under the assumption of diluted distribution. The solved mean free path of electron defines a length scale that fixes the "threshold" of applied electrical load that causes crack tip melting, defines the applicable domain of macroscopic mean field solutions, and provides an estimate of crack tip radius when it is unknown.

Appendix I: Solutions of Problems II, III in Fig. 4a,b

According to the method introduced by Mushelishivili [21], the solutions for the problem II in Fig. 4a or problem III in Fig. 4b can be derived by the following procedure:

Build the analytical function by electrical potential φ and magnetic field H_3:

$$F(z) = -\varphi + i\frac{H_3}{\sigma^C}, \tag{a1}$$

Its derivative is electrical field:

$$\frac{dF(z)}{dz} = E_x - iE_y \tag{a2}$$

because

$$\frac{dF(z)}{dz} = \left[\frac{dF(z)}{dz}\right]_{dz=dx} = \left[\frac{dF(z)}{dz}\right]_{dz=idy}$$

and

$$\left[\frac{dF(z)}{dz}\right]_{dz=dx} = -\frac{\partial\varphi}{\partial x} + i\frac{\partial H_3}{\sigma^C \partial x}, \qquad \left[\frac{dF(z)}{dz}\right]_{dz=idy} = -\frac{\partial\varphi}{i\partial y} + \frac{\partial H_3}{\sigma^C \partial y}$$

According to Cauchy-Riemann's condition:

$$\frac{\partial}{\partial x}(-\varphi) = \frac{\partial}{\partial y}\left(\frac{H_3}{\sigma^C}\right), \qquad \frac{\partial}{\partial y}(-\varphi) = -\frac{\partial}{\partial x}\left(\frac{H_3}{\sigma^C}\right)$$

Notice that $\frac{1}{i} = -i$, (a2) is proven.

According to Mushelishivili [21]:

$$\frac{dF(z)}{dz} = \frac{1}{\pi\sqrt{z^2 - a^2}} \int_{-a}^{a} \frac{p(z)\sqrt{\varsigma^2 - a^2}}{\varsigma - z} d\varsigma + \frac{P(z)}{\sqrt{z^2 - a^2}} \tag{a3}$$

where $p(z)$ is the electrical current imposed on crack surface; $P(z) = C_0 + zC_1 + z^2C_2 + ... + z^nC_n$ where the order n and coefficients C_i, $i = 1,2,...,n$ are to be determined according to remote boundary condition. The Cauchy integral in (a2) can be solved analytically, see the Appendix of [69].

Appendix II Feromagnetic and Antiferromagnetic phases of Iron [46]

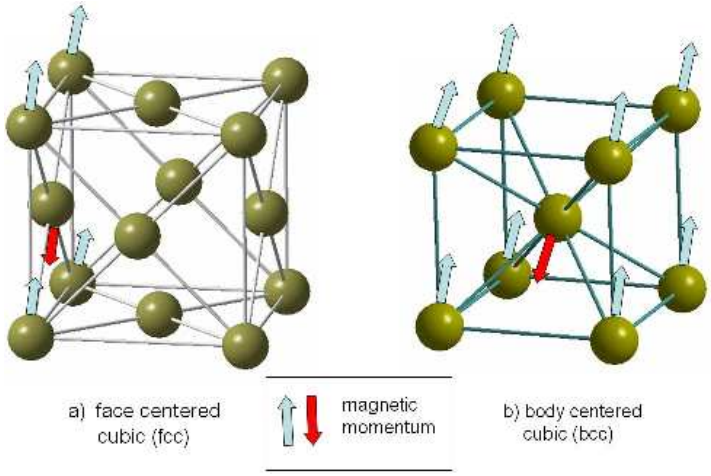

Fig. II-1: Unit cells of fcc (austenite, γ phase) and bcc (ferrite/martensite, α/α' phase) crystal; the transformation between them defines "martensitic transformation"

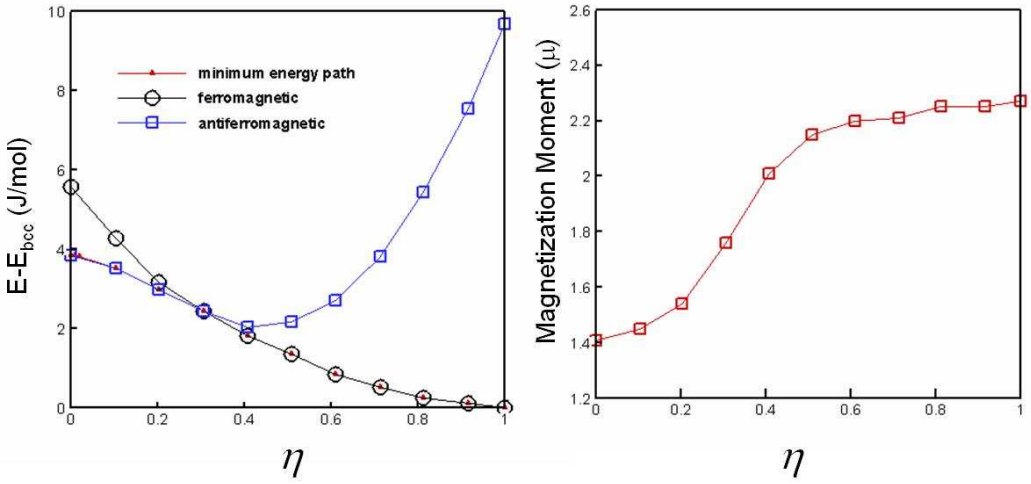

(a) (b)

Fig. II-2 Quantum mechanical computations of the unit atomic cell during fcc-bcc transformation where η is the order parameter of lattice constant ($\eta = 0$: fcc, $\eta = 1$: bcc). (a) changes of system energies; the minimum energy path is the actual path of martensitic transformation; (b) variations of magnetic moment per atom.

Acknowledgements. This research is partially sponsored by the US Office of Naval Research, Project Officer: Dr. Schmidt. The author would like to express his sincere gratitude to the support. The author would like to thank Professor Q. Wang of the Department of Mechanical Engineering, Northwestern University for her helps in carefully review of the the manuscript and many beneficial suggestions, to Professor J. B. Ketterson, Physics and Astronomy Department of Northwestern University for the illuminated discussion in the early stage of this research, to Professor L. M. Keer of the Department of Mechanical Engineering, Northwestern University, Dr. S. Satapathy of the Institute of Advanced Technology, University of Texas at Austin, for their kind supports and many beneficial discussions.

References

1. Laudau, L.D., Lifshitz, E. M. and Pitaevskii, L. P., *Electrodynamics of Continuous Media*. Vol. 8. 1960: Pergamon Press.
2. Jackson, D., *Classical Elastodynamics*. 3 ed. 1975.
3. Knoepfel, H., *Magnetic Field: A Comprehesive Theoretical Treatise for Practical Use*. 2000, New York: Wiley.
4. Garboczi, E.J., *Linear Dielectric-Breakdown Electrostatics.* Physical Review B, 1988. **38**(13): p. 9005-9010.
5. Satapathy, S., F. Stefani, and A. Saenz, *Crack tip behavior under pulsed electromagnetic loading.* IEEE Transactions on Magnetics, 2005. **41**(1): p. 226-230.
6. Persad, C., et al., *On the nature of the armature-rail interface: Liquid metal effects.* IEEE Transactions on Magnetics, 1997. **33**(1): p. 140-145.
7. Freund, L.B., *The mechanics of electronic materials.* International Journal of Solids and Structures, 2000. **37**(1-2): p. 185-196.
8. Dorighi, J., Krishnaswamy, S., Achenbach, J. , *A fiber optic ultrasonic system to monitor the cure of epoxy* Res. Nondestructive Evaluation 1997. **9**(1): p. 13-24.
9. Achenbach, J.D., *The thermoelasticity of laser-based ultrasonics* J. Thermal Stress, 2005. **28**(6-7): p. 713-727.
10. Jiles, D. C., *Theory of the Magnetomechanical Effects.* J. Physics D., 1995. **28**(8): p. 1537-1546.
11. Wang, B.L., Mai, Y. W., *Impermeable crack and permeable crack assumptions, which one is more realistic?* J. Appl. Mech., 2004. **71**(4): p. 575-578.
12. Huang, J.H. and W.S. Kuo, *The analysis of piezoelectric/piezomagnetic composite materials containing ellipsoidal inclusions - Reply.* Journal of Applied Physics, 1997. **82**(10): p. 5270-5270.
13. Huang, J.H., *Analytical predictions for the magnetoelectric coupling in piezomagnetic materials reinforced by piezoelectric ellipsoidal inclusions.* Physical Review B, 1998. **58**(1): p. 12-15.
14. Chung, M.Y., Ting, T. C. T., *The Green function for a piezoelectric piezomagnetic magnetoelectric anisotropic elastic medium with an elliptic hole or rigid inclusion.* J. Appl. Mech., 1995. **72**(6): p. 405-410.
15. Wang, B.L., Mai, Y. W., *Closed-form solution for an antiplane interface crack between two dissimilar* J. Appl. Mech., 2006. **73**(2): p. 281-290.
16. Ashcroft, N.W., Mermin, N. D., *Solid State Physics*. 1976, Fort Worth: Saunders College Publishing.
17. Bilby, B.A., Cottrell, A. H., Swinden, K. H., *The Spread of Plastic Yield from a Notch.* Proc. Roy. Soc. London, 1963. **A272**: p. 304-314.
18. Dugdale, D.S., *Yielding of Steel Sheets Containing Slits.* J. Mech. Phys. Solids, 1960. **8**: p. 100-108.
19. Gao, H.J., Zhang, T. Y., Tong, P., *Local and Global Energy Release Rate for Electrically Yielded Crack in a Piezoelectric Ceramic*. J. Mech. Phys. Solids, 1997. **45**: p. 491-510.
20. Horowitz, G.E., *(in German).* Arch. Elecktrotech. Berlin, 1927. **18**.
21. Mushelishivili, N.I., *Some Basic Problems of Mathematical Theory of Elasticity*. 1953, Groningen. Holland.

22. Liebowitz, H., *Fracture, An Advanced Treatise. Edited by H. Liebowitz*. 1968, New York: Academic Press.
23. Sih, G.C., *Application of Muskhelishvili's Method to Fracture Mechanics.* Transaction, The Chinese Assn. for Advanced Studies, 1962: p. 25-55.
24. Erdogan, F. *On the Stress Distribution on Plates with Collinear Cuts under Arbitrary Loads*. in *The Fourth U. S. National Congress of Applied Mechanics*. 1962.
25. Davies, D.K., Biondi, M. F., *Vacuum Breakdown between Plane-parallel Copper Plate.* J. Appl. Physics, 1966. **37**(8): p. 2969-2977.
26. Taylor, E.D., P.G. Slade, and M.B. Schulman, *Transition to the diffuse mode for high-current drawn arcs in vacuum with an axial magnetic field.* IEEE Transactions on Plasma Science, 2003. **31**(5): p. 909-917.
27. Weertman J., W., J. R., *Elementary Dislocation Theory* 1964, New York: Macmillan.
28. Rice, J.R., *A Path Independent Integral and Approximate Analysis of Strain Concentration by Notches and Cracks.* Journal of Applied Mechanics, 1968. **35**(2): p. 379-&.
29. West, A.R., *Solid State Chemistry and Its Applications*. 1984, Chichester: Wiley.
30. Galway, A.K., *A view and a review of the melting of alkali metal halide crystals.* J. Thermal Analysis and Calorimetry, 2005. **82**: p. 23-40.
31. Kittel, C., *Introduction to Solid State Physics*. 7 ed. 2002, Singapore, New York: John Wiley & Son.
32. Fleck, N.A., Muller, G.M., Ashby, M.F., and Hutchinson, J.W., *Strain Gradient Plasticity: Theory and Experiment.* Acta Metallurgica et Materialia, 1994. **42**: p. 475-487.
33. Fleck, N.A., and Hutchinson, J.W., *Strain gradient plasticity.* Advances in Applied Mechanics, 1997. **33**: p. 295-361.
34. Gao, H.J., Huang, Y., Nix, W.D., and Hutchinson, J.W., *Mechanism-Based Strain Gradient Plasticity - I. Theory.* Journal of Mechanics and Physics of Solids, 1999. **47**: p. 1239-1263.
35. Lemonds, J., and Needleman, A., *An analysis of shear band development incorporating heat-conduction.* Mech. Mater, 1986. **5**: p. 363-373.
36. Belytschko, T., Gu, L., and Lu, Y. Y., *Fracture and Crack-Growth by Element Free Galerkin Methods.* Modelling and Simulation in Materials Science and Engineering, 1994. **2**(3A): p. 519-534.
37. Bardeen, J.a.S., W., *Deformation potential and mobilities in non-polar crystals.* Phys. Rev., 1950. **80**: p. 72-80.
38. Slater, J.C., *Electrons in Perturbed Periodic Lattices.* Phys. Rev., 1949. **76**(11): p. 1592-1561.
39. Fonseca, L.R.C., et al., *Self-consistent calculation of the electronic structure and electron-electron interaction in self-assembled InAs-GaAs quantum dot structures.* Physical Review B, 1998. **57**(7): p. 4017-4026.
40. Leburton, J.P., et al., *Electronic properties and mid-infrared transitions in self-assembled quantum dots.* Japanese Journal of Applied Physics Part 1-Regular Papers Short Notes & Review Papers, 1999. **38**(1B): p. 357-365.
41. Pryor, C., et al., *Comparison of two methods for describing the strain profiles in quantum dots.* Journal of Applied Physics, 1998. **83**(5): p. 2548-2554.
42. Eshelby, J.D., *Elastic inclusions and inhomogeneities* in *Progress in Solid Mechanics*, I.N. Sneddon, Hill, R., Editor. 1961, North-Holland: Amsterdam. p. 89-140.

43. Paschen, F., *Ueber die zum Funkenuebergang in Luft, Wasserstoff and Kohlensaeure bei verschiedenen Druecken erforderliche Potentialdifferenz (in German).* Weid. Annalen der Physick, 1889. **37**: p. 69-75.
44. Slade, P.G. and E.D. Taylor, *Electrical breakdown in atmospheric air between closely spaced (0.2 mu m-40 mu m) electrical contacts.* IEEE Transactions on Components and Packaging Technologies, 2002. **25**(3): p. 390-396.
45. Johanson, G.J., McGirr, M. B., *Determination of the Neel Temperature of Face-Centered-Cubic Iron.* Physical Review B, 1970. **1**(7): p. 3208-3208.
46. Hao, S., Olson, G. B., *Multi-Scale Mechanical Optimization for Design of High Strength, High Toughness Austenite-Martensite Alloys (manuscript submitted)* in *The 5th International Conference on Martensite Transformation (ICOMAT05)*. 2005: Shang Hai, China.
47. Rice, J.R., *Dislocation Nucleation from a Crack Tip* J. Mechanics and Physics of Solids 1992. **40**(2): p. 239-271.
48. Gallo, F., Watkins, R., Ravi-Chander, K., Satapathy, S., F., *Strain R-Evolution in Metal Conductors Subjected to Short-Duration Current Pulses,* IEEE Transactions on Magnetics, 2007. **43**(1): p. 338-342.
49. Brown, L., Xu, D., Ravi-Chander, K., Satapathy, S., F., *Coefficient of Friction Measurement in the Presence of High Current Density,* IEEE Transactions on Magnetics, 2007. **43**(1): p. 334-337.
50. Hoffman C. A., Meyer J. R., Bartoli F. J., Di Venere A., Yi XJ, Hou C. L, Wang H. C., Ketterson J. B., Wong G. K., *Semimetal-to-Semiconductor Transition in Bismuth Thin-Films.* Physical Review B, 1993. **48**(15): p. 11431-11434.
51. Shafranjuk, S.E. and J.B. Ketterson, *Resonant states of a double-barrier junction.* Physical Review B, 2005. **72**(2): 024509 p. 1-9.
52. Chen, Y., Snyder, J.E., Schwichtenberg, C. R., Dennis, K. W., Falzgraf, D. K., McCallum, R. W., Jiles, D. C., *Effect of the elastic modulus of the matrix on magnetostrictive strain in composites.* Appl. Phys. Letters, 1999. **74**(8): p. 1159- 1161.
53. Shi, Y., Jiles, D. C., *Finite Element Analysis of the Influence of a Fatigue Crack on Magnetic Properties of Steel.* J. Appl. Phys., 1998. **83**(11): p. 6353-6355.
54. Pak, Y.E., *Crack extension force in a piezoelectric material.* J. Appl. Mech., 1990. **57**(3): p. 647-653.
55. Keer, L.M., et al., *Simulation of Wear Particle Creation in Asperity Contacts Using the Finite-Element Method.* Tribology Transactions, 1993. **36**(4): p. 613-620.
56. Liu, G., Q. Wang, and S.B. Liu, *A three-dimensional thermal-mechanical asperity contact model for two nominally flat surfaces in contact.* Journal of Tribology-Transactions of the ASME, 2001. **123**(3): p. 595-602.
57. Hao, S. and Keer, L. M., *Rolling Contact between Rigid Cylinder and Semi-infinite Elastic Body with Sliding and Adhesion.* Journal of Tribology-Transactions of the ASME, 2007. **129**(3).
58. Sablik, M. J., *A Model for Asymmetry in Magnetic Property Behavior under Tensile and Compressive Stress in Steel.* IEEE Transactions on Magnetics, 1997. **33**(5): p. 3958-3960.
59. Sablik, M. J. and Jiles, D. C., *Coupled Magnetoelastic Theory of Magnetic and Magnetostrictive Hysteresis.* IEEE Transactions on Magnetics, 1993. **29**(3): p. 2113-2123.
60. Hoffmann, A., *Symmetry Driven Irreversibilities at Ferromagnetic-Antiferromagnetic Interface.* Phy. Rev. Lett., 2004. **93**(9), 097203.

61. McMeeking, R. M., *Electrostrictive Stress near Crack-Like Flaws.* Zeitschrift fur Ange. Math. Phy., 1989. **40**(5), 615-627.
62. Suo, Z., Kuo, C. –M., Barnett, D. M., Willis, J. R., *Fracture Mechanics for Piezoelectric Solids.* J. Mech. Phys. Solids, 1992. **40**, 739-765
63. Suo Z., *Models for Breakdown-Resistant Dielectric and Ferroelectric Ceramics.* J. Mech. Phys. Solids, 1992. **41**, 1155-1176.
64. McMeeking, R. M., *On Mechanical Stress at Cracks in Dielectrics with Applications to Dielectric Breakdown*., J. Appl. Phys., 1987. **62**(8), 3116-3118
65. Gleskova H., Wagner S., Soboyejo W., Suo Z., *Electrical Response of Amorphous Silicon Thin-Film Transistors under Mechanical Strain*., J. Appl. Phys., 2002. **92**(10), 6224-6229.
66. Pak Ye, *Crack Extension Force in a Piezoelectricl Material.* J. Appl. Mech., 1990. **57**(3), 647-653.
67. Schneider C. S., Cannell P. Y., Watts K. T., Magnetoelasticity for Large Stress, IEEE Transactions on Magnetics, 1992. **28**(5): p. 2626-2631.
68. Rice J. R., Johnson M. A., *Inelastic Behavior of Solids.* Edtors. M. F. Kanninen, et. al., McGraw Hill, 1970, p.641-659.
69. Weertman, J., *Dislocation Based Fracture Mechanics*. 1996, London: World Scientific.
70. Achanta R. S., Plawsky J. L., Gill W. N., *A Time Dependent Dielectric Breakdown Model for Field Accelerated Low-k Breakdown Due to Copper Ions*, J. Applied Phys., 2007, 91, 234106.
71. Lee B. H., Kang C. Y., Kirsch P., Heh D., Yong C. D., Park H., Yang J., Bersuker G., Electric-Field-Driven Dielectric Breakdown of Metal-Insulator-Metal Hafnium Silicate, Applied Phys. Letters, 2007, 91, 233514.